The role of gravitational collapse in controlling the evolution of crestal fault systems (Espírito Santo Basin, SE Brazil)

Tao Ze[1*], Tiago M. Alves[1]

[1]3D Seismic Lab, School of Earth and Ocean Sciences, Cardiff University, Main Building, Park Place, Cardiff, CF10 3AT, United Kingdom

Corresponding author: Tel: (+44)07421148109; E-mail: taoz@cardiff.ac.uk

Abstract

A high-quality 3D seismic volume from offshore Espírito Santo Basin (SE Brazil) is used to assess the importance of gravitational collapse in the formation of crestal faults above salt structures. A crestal fault system is imaged in detail using seismic attributes such as curvature and variance, which are later complemented by analyses of throw vs. distance (T-D) and throw vs. depth (T-Z). In the study area, crestal faults comprise closely spaced arrays and are bounded by large listric faults, herein called *border faults*. Two episodes of growth are identified in two opposite-dipping fault families separated by a transverse accommodation zone. Statistical analyses for eighty-four (84) faults show that fault spacing is < 250 m, with border faults showing the larger throw values. Fault throw varies between 8 ms and 90 ms for crestal faults, and 60-90 ms for border faults. Fault length varies between ~410 m and 1750 m, with border faults ranging from 1250 m to 1750 m. This work shows that border faults accommodated most of the strain associated with salt growth and collapse. The growth history of crestal faults favours an isolated fault propagation model with fault segment linkage associated with the lateral propagation of discrete fault segments. Importantly, two episodes of fault growth are identified as synchronous to two phases of seafloor erosion, rendering local unconformities as competent markers of fault reactivation at a local scale.

This paper has crucial implications to the understanding of fault growth histories as a means to assess drilling risk and oil and gas migration on continental margins with important salt tectonics. As a corollary, this work demonstrates that: 1) a certain degree of spatial organization occurs in crestal fault systems; 2) transverse accommodation zones can form regions in which fault propagation is enhanced and where regional dips of faults change in 4D.

Keywords: SE Brazil; salt tectonics; crestal faults; fault reactivation; fault propagation; accommodation zones.

1. Introduction

Crestal faults comprise a group of faults rooted in the crest of salt diapirs (Jenyon, 1988; Randles et al., 2012). Despite their occurrence in multiple salt-rich basins, few studies have focused on the kinematic and dynamic evolution of crestal faults, in part because very few regions in the world fully expose these faults at outcrop. Good exposure of salt diapirs' flanks is chiefly recorded in the Paradox Basin, Utah (Furuya et al., 2007), Colorado (Gutiérrez, 2004), La Popa Basin in Mexico (Rowan et al., 2003) and the Dead Sea basin (Alsop et al., 2015). These outcrops essentially reveal the main boundary faults of crestal fault systems, but erosion often obliterates the fault families formed directly above growing salt structures. In parallel, diffraction and loss of signal around salt diapirs make most crestal faults hard to image on seismic data. With deeper burial depths, vertical and horizontal seismic resolutions can also be significantly reduced (Davison et al., 2000).

Important new findings have occurred in the last few decades in terms of evaluating fault growth history through seismic, outcrop, numerical and analogue modelling data (Alves, 2012; Bose and Mitra, 2010; Cartwright, 2011; Cartwright et al., 2000; Cartwright et al., 1995; Childs et al., 2009; Clausen et al., 2014; Cowie and Scholz, 1992; Garcia et al., 2012; Jackson and Larsen, 2009; Jackson and Rotevatn, 2013; McLeod et al., 2000; Morley, 2007; Yin and Groshong, 2007). The early fault growth model of Barnett et al. (1987) was initially proposed to represent isolated normal faults propagating in a radial direction, and records no migration of maximum displacement points. Recent work focused on documenting changes in the dimensions and absolute fault displacements to build more reliable fault-propagation models (Mansfield and Cartwright, 2001; Walsh et al., 2002b). It is now recognised that mature faults are a result of fault-segment linkage associated with the propagation in both the vertical and horizontal directions (Cartwright et al., 1995; Cowie et al., 2000; Lohr et al., 2008; Stewart et al., 1997). Following the latter concepts, Jackson and Rotevatn (2013) summarized two mechanisms of normal fault propagation in 'isolated' fault and 'coherent' fault models. The isolated fault model is supported by many researchers, but recent work stress that the coherent fault model is the dominant fault growth process in many an extensional setting (Morley, 1999; Walsh et al., 2003; Walsh et al., 2002a). In the 'coherent' model, faults first propagate laterally to reach a length close to their maximum and record cumulative displacement in a second throw-dominated stage. A supplementary model has been presented by Lohr et al. (2008), who demonstrated that most faults grow by the coalescence of several smaller faults, whereas tip propagation is of relatively minor importance. Acknowledging this latter process of fault growth, Cartwright et al. (2000), McLeod et al. (2000) and Sibson (1985) argued that the geometry of large faults is essentially controlled by several small existing fault segments, rather than by a large fault created at quasi-instantaneous geological scales. Against this backdrop, the propagation history of crestal fault families is still poorly understood, and is thus examined in detail in this paper.

An important concept in this paper is that of *border faults*. The concept was first introduced for rift basins as normal faults forming escarpments on their shoulders (Crossley and Crow, 1980), often with large displacement and length (Ebinger et al., 1987), and accommodating most strain and stress. Boundary faults in salt tectonics are also a type of border fault following this criteria (Randles et al., 2012). This paper follows the concept that faults with the largest displacement and throw values within a crestal fault family comprise border faults.

Accommodation (or transfer) zones are also important structures revealed in this study. Previous studies on accommodation zones have largely focused on large-scale rift basins in the scale of 10s and 100s of kilometres (Coffield, 1987; Morley et al., 1990; Smith et al., 2001). However, accommodation zones can occur at different scales (Fossen and Rotevatn, 2016; Liu et al., 2015; Schlische and Withjack, 2009) and in different regimes and settings, such as in areas of significant salt tectonics (Randles et al., 2012). In this study we follow the definition of Faulds and Varga (1998), who considered accommodation zones as structures that accommodate strain and stress between overlapping normal faults systems, or families. In the published literature, accommodation zones generated during the propagation of normal faults have an important control on the sub-surface distribution of hydrocarbons by: a) influencing the deposition of reservoir and source rocks, b) facilitating or restricting fluid migration, and c) forming structural traps (Langhi and Borel, 2008; Morley et al., 1990).

Crestal faults are important structures as they deform strata on the crests of growing salt diapirs, forming natural traps where fluids can accumulate (Baars and Stevenson, 1982; Rowan et al., 1999). Fault systems developed on the crest of salt structures can also generate surface topography, leading to significant erosion on the seafloor; in fact, the movement of crestal faults is an important trigger of submarine landslides and channel erosion on continental slopes (Gee and Gawthorpe, 2006). Crestal faults are also important elements of structural traps associated with salt diapirs, either enhancing reservoir porosity or, instead, acting as conduits for sub-surface fluid (Cartwright et al., 2007; Gay et al., 2007). An important feature of crestal faults is their ability to grow (and reactivate) during successive episodes of crestal collapse (Walsh et al., 2002b). Thus, systematic studies of crestal faults have practical implications in assessing geohazards (Lisle and Srivastava, 2004), fault seal competence (Holdsworth et al., 1997), and CO_2 sequestration in regions of significant salt tectonics (Jung et al., 2014; Van der Veer, 2013).

The study area, located in ultra-deep areas of the Espírito Santo Basin, SE Brazil (Fig. 1b), reveals the development of large salt walls and diapirs (Gamboa et al., 2010a) (Fig. 1c). Here, the continental slope is deformed by growing NW- and NE-trending salt structures (Fig. 1c), and local processes such as slope instability and submarine channel incision are associated with the development of near-seafloor fault systems (Gamboa et al., 2010a; Omosanya and Alves, 2014). Previous work showed that halokinesis can generate extensional faults on top of rising salt anticlines, with subsequent mass-transport deposits (MTDs) and channels marking the last stages of fault growth over active salt structures (Alves, 2012; Alves and Cartwright, 2009; Baudon and Cartwright, 2008b). A multi-stage evolution is therefore expected, in the study area, for crestal faults generated above active salt structures (Baudon and Cartwright, 2008b).

This paper presents new data on fault families developed over the crest of a salt ridge in SE Brazil (Fig. 1c). An accommodation zone kinematically and dynamically linked with the interpreted crestal fault families is documented for the first time on a developed salt structure. Opposite-dipping fault families, and the associated accommodation zone, are analysed using a high-resolution 3D seismic volume with a vertical resolution approaching 8-10 m near the seafloor. In summary, this study aims to:

a) Document the geometry of fault families developed above a well-imaged salt ridge in SE Brazil;

b) Analyse the growth and reactivation histories of crestal fault families and the role of border faults exerting on the fault system, extrapolating the results to salt structures on other continental margins;

c) Examine the style(s) of propagation of crestal fault families, and their relationship with stratigraphic unconformities developed above the interpreted faults.

2. Geological setting

Sedimentary basins formed along the continental margin of SE Brazil are associated with rifting and break-up of the Gondwana supercontinent (Cainelli and Mohriak, 1999; Chang et al., 1988; Fiduk et al., 2004; Hung Kiang Chang et al., 1992; Ojeda, 1982). Continental break-up between Brazil and Africa evolved gradually from the southern part of the Atlantic Ocean towards the north (Chang et al., 1992). In such a setting, the Espírito Santo Basin was formed in the Late Jurassic-Early Cretaceous as a rift basin filled with continental and lacustrine deposits (Chang et al., 1992; Mohriak et al., 2008). The basin evolved towards a fully rifted passive margin after the Aptian; therefore, strata in the study area can be grouped into five megasequences: i) continental syn-rift; ii) transitional evaporites; iii) shallow marine carbonate platform; iv) open marine transgressive and v) regressive (Chang et al., 1988).

Early post-rift strata in the Espírito Santo Basin chiefly comprise Late Aptian evaporites (Demercian et al., 1993; Mohriak et al., 2008; Ojeda, 1982). Accumulated evaporites include anhydrite, halite, carnalite, sylvinite and tachyhydrite (Ojeda, 1982). As the basin deepened, the progradation of strata from shallower proximal areas of the margin triggered widespread halokinesis on the continental slope (Demercian et al., 1993). Thin-skinned gravitational gliding over Aptian evaporites (Demercian et al., 1993; Fiduk et al., 2004) is recognised as the main trigger of salt tectonics throughout SE Brazil (Demercian et al., 1993; Vendeville and Jackson, 1992a,b). Salt deformation mechanisms also include differential loading by overburden strata (Omosanya and Alves, 2013). As a result, halokinesis in the Espírito Santo Basin peaked during the Late Cenozoic and is still important at present (Fiduk et al., 2004).

Due to progressive eastward tilting and continuous subsidence (Bruhn and Walker, 1997), three structural domains are observed at present in the Espírito Santo Basin: a) proximal extensional, b) transitional and c) distal compressional (Fig. 2) (Gamboa et al., 2010b; Mohriak et al., 2012; Rouby et al., 2003; Vendeville, 2005). Main structures in the extensional domain include salt rollers, salt walls along conjugate normal faults, turtle anticlines and rafts (Mohriak et al., 2008). The transitional domain is dominated by salt diapirs, whereas the compressional domain comprises allochthonous salt (Davison, 2007; Demercian et al., 1993). Crestal fault families are developed on collapsed salt diapirs and on salt ridges generated in the transitional and compressional domains (Alves, 2012; Alves et al., 2009).

The study area is located in the compressional regime of the Espírito Santo Basin, where salt-withdraw basins developed due to the growth of allochthonous salt ridges and diapirs (Figs. 1 and 2). The studied fault system is located above a prominent N-striking salt ridge with a developed depression above (Figs. 1 and 3). The bottom of the salt ridge is absent with the studied seismic volume (Fig. 4); however, active salt diapirism is revealed by the presence of an active salt intrusion that noticeably deformed the seafloor (Fig. 4).

3. Data and methods

This paper uses a 3D seismic volume covering ~1800 km^2 of the Espírito Santo Basin, in SE Brazil, at a minimum water depth of 1600 m (Fig. 1b). The study area is bounded by the Abrolhos Bank to the north and by the Vitória-Trindade Chain to the East (Fig. 1b). Seismic data processing included resampling, spherical divergence corrections and zero-phase conversions, which were undertaken prior to stacking, 3D pre-stack time migration using the Stolt algorithm (Stolt and Benson, 1986) and one-pass 3D migration. The vertical sampling rate for the interpreted seismic volume is 2 ms and its bin spacing is 12.5 m. With a dominant frequency of 40 Hz, the vertical resolution is estimated to be between 8-10 m near the seafloor and 20 m at the maximum depth of strata investigated in this work.

The study area is located on a prominent NW-SE trending salt ridge with a width of 4 km wide and a length of over 30 km (Fig. 1c). This salt ridge separates two NE–trending salt-withdrawal basins (Fig. 1c). Interpretation of seismic data was performed using Petrel®; thus, seven (7) key horizons were mapped over the salt ridge to constrain the main episodes of fault reactivation. Constraints on the age of the stratigraphy units are based on published literature (Alves et al., 2009; Baudon and Cartwright, 2008b; Fiduk et al., 2004). In addition, seismic attributes such as variance and curvature were used to identify any relevant structural features (Chopra and Marfurt, 2007; Rijks and Jauffred, 1991). In the study area, swarms of faults are clearly observed in selected variance and surface maps (Figs. 1d and 3).

Fault throw plots are used in this paper to evaluate fault growth history with some important remarks: 1) the seismic volume is in time domain; 2) the surfaces of the faults are relatively smooth and only slightly listric; 3) throw-depth plots are effectively used to recognise key reactivation episodes here in this study; 4) maximum thickness of sediment on crest of the studied area is ~1250 meters (given a compressional velocity of 2500m/s on average for the first 1250 meters) and the strata is highly faulted and filled with pore fluid. This character implies that, for the first 1000 meters below the seafloor, variations in compressional velocity have less influence on fault throw plots than in deeper strata (Alves et al., 2009; Leyden et al., 1972; Storvoll et al., 2005).

Stereogram plots showing the strike direction and dip angle of faults were produced on 3D Move®, which divides a single fault surface into a number of triangular surfaces. The number of triangular surfaces depends on the sticks and pillars interpreted on, and exported from Petrel®. Fault density is calculated based on the number of seismically resolved faults along seismic sections. The Expansion Index, which represents the thickness ratio between strata on hanging-wall and footwall blocks, is used to identify episodes of fault growth (Lewis et al., 2013; Mansfield and Cartwright, 1996). Nucleation of maximum throw depth vs. seismic horizons is used in this study to characterise the relative timing of distinct fault sets (Alves, 2012).

The studied fault families were divided into three zones; a northernmost zone with chiefly E-dipping faults (Zone 1), a middle part intersected by a prominent accommodation zone (Zone 2), and a southernmost zone with W-dipping faults (Zone 3) (Figs. 3 and 4).

4. Seismic stratigraphy

In the study area, strata can be divided into four seismic-stratigraphic units, which are bounded by seven horizons (H1 to H7). Horizon H1 represents the top of the Aptian salt, whereas H7 represents the seafloor (Fig. 5). Additionally, four seismic horizons (H2-1 to H2-4) are interpreted between Horizon H2 and H3 to constrain the Expansion Index of faults (Fig. 5b). Seismic-stratigraphic interpretations were extended to the adjacent salt-withdrawal basin in order to constrain the age of the strata on the crest of the salt ridge (Fig. 5a).

4.1 Unit 1 (Early Eocene?)

Unit 1 is bounded by H2 at its top and is characterised by strong to moderate amplitude internal reflections, which are chaotic at places (Fig. 5a). The bottom of Unit 1 is hardly identified in the adjacent salt-withdrawal basin. Its top (H2) coincides with a regional unconformity of Mid-Eocene age (Fiduk et al., 2004; Gamboa and Alves, 2015). This thin unit (< 250 ms TWT, approximately 312.5m given a compressional velocity of 2000m/s for sediment on crest of the salt diapir) developed on top of the salt ridge comprises remnants of Lower Eocene strata, hinting at continuous salt growth since the Late Cretaceous. In the salt-withdrawal basin, synclinal faults are developed in Unit, which are related to a synclinal fold *sensu* Alves (2012) (Fig. 5a).

4.2 Unit 2 (Middle Eocene - Oligocene)

Unit 2 is bounded at its base by a mid-Eocene unconformity (H2) and at its top by Horizon H3 (Fig. 5). Strata within this unit show sub-parallel, high-amplitude internal reflections with good lateral continuity (Fig. 5). High-amplitude reflections in this unit are generated by volcaniclastic material sourced from the Abrolhos Bank during the Middle Eocene-Oligocene (Fiduk et al., 2004; Gamboa et al., 2010a). Mass-transport deposits showing chaotic internal reflections are common on the flanks of the interpreted salt ridge (Fig. 5a).

Unit 2 is faulted on the crest of the salt ridge (Fig. 5b) and thins sharply towards the east on top of this same ridge (Fig. 5).

4.3 Unit 3 (Miocene)

Unit 3 is bounded by a moderate and continuous seismic reflection at its top (Horizon H4, Fig. 5). Internal reflections vary in character over the salt ridge, in Unit 3, when compared to the adjacent salt-withdrawal basins (Fig. 5a). The unit is characterised by transparent to low amplitude internal reflections over the salt ridge, but shows strong reflections in the salt-withdrawal basin. Strata in these confining basins onlap the salt ridge (Fig. 5a). The contrast in thickness between the crest of the salt ridge and equivalent strata in the salt-withdrawal basins reflects an important episode of salt growth during the Middle-Late Miocene, after which halokinesis weakened in the study area (Fiduk et al., 2004). As shown in Figure 5a, strata above H2 in the salt-withdraw basin is thicker, with ~1400 ms (TWT) compared with a maximum of ~700 ms (TWT) on the crest of salt diapir. The contrast in thickness between the two areas is partly due to collapse and erosion on top of the salt ridge, which resulted in the accumulation of MTDs in the salt-withdraw basin and on the formation of a correlative erosional surface (Horizon 5) on top of the salt ridge (Fig. 5a).

4.4 Unit 4 (Late Miocene - Quaternary)

Unit 4 shows internal seismic reflections of moderate amplitude and is divided into three sub-units (Fig. 5). The lowermost sub-unit 4a is bounded at its base by Horizon H4 and at its top by H5 (Fig. 5). A large number of crestal faults terminate at H5 (Fig. 5b). The intermediate sub-unit 4b is bounded at its top by an onlap surface (Horizon H6; Fig. 5a). Very few faults are developed in sub-unit 4b, but fault-related folding of the modern seafloor is markedly observed (Fig. 5b). The uppermost sub-unit 4c extends to the seafloor (Horizon 7). Few faults propagate to the seafloor in sub-unit 4c (Figs. 4 and 5).

5. Fault geometry

5.1 Fault geometry and density

Interpreted crestal fault families can be subdivided into four groups according to the relative depth in which their upper tips terminate (Figs. 4, 5b and 6). Group 1 contains faults that offset Horizon H5, a main erosional surface developed over the salt ridge (Fig. 4a). A few of the faults in Group 1 reach the seafloor (Figs. 4, 5b and 6), a character indicating active salt diapirism (Fiduk et al., 2004). Group 2 faults comprise faults that offset H4 but terminate beneath H5, with Horizon H4 comprising a major truncation surface at the bottom of Unit 3 (Figs. 4, 5b and 6). Group 3 faults comprise structures that offset the top of Unit 1 (Horizon H3) and terminate within Unit 2 (Figs. 4, 5 and 6). Group 4 faults are confined to Unit 2 (Figs. 4a and 6).

Faults in Groups 1 and 2 show approximately the same number, respectively 30 and 29 faults. Group 1 comprises the faults with the largest displacements in the study area (Figs. 4 and 5). Group 4 faults are rare, with only a few being imaged within a central depression developed on the crest of the salt ridge (Fig. 6). These latter faults show the smallest length and displacement values (Figs. 3, 4 and 5). All in all, the four groups of faults form two distinct fault families towards the northern (Zone 1) and southern (Zone 3) halves of the interpreted salt ridge (Figs. 3 and 4).

Fault 1A and 2A in Zone 1, where faults in each Group are named by capital letters preceded by numbers showing fault group, show the largest displacement and throw values. Based on the criteria that faults with the largest displacement and length accommodate the bulk of strain and stress, faults 1A and 2A are interpreted to form border faults in Zone 1. Following the same criteria, faults 1E and 1G are considered to form border faults in Zone 3 (see details of maximum throw of these faults in section 6).

Faults in Zone 1 dip to the east, with a few antithetic faults occurring at the edge of the salt ridge and forming graben-like structures (Fig. 4a). The average strike of faults dipping to the east in Zone 1 is 354.74^0 NNW and their average dip angle approaches 35.37^0 (Fig. 7a). Border fault 1 (BF1) strikes N-S close to Zone 2, but gradually changes its strike to NNE into Zone 1 (Fig. 3). Border Fault 2 (BF2) changes its strike from NNW to NNE in a south to north direction (Fig. 3). Both border faults are listric, dipping to the east (Fig. 4a). Antithetic faults in Zone 1 show an average strike of 20.31^0 NNE and an average dip angle of 36.7^0 (Fig. 7b). In contrast to the northern part of the salt ridge, faults in Zone 3 dip uniformly to the west. Their average strike direction is 5.34^0 NNE and the average dip angle is 35.94^0 (Fig. 7c). Border faults 1E and 1G also strike NNE (Fig. 3). Most of the faults in Zone 3 are listric and slightly curved in map view (Figs. 3 and 4b).

Figure 8 presents the density of seismically resolved faults for the study area. Figure 8a separately shows fault density on the hanging-wall and footwall blocks of BF1, from south to north (Figs. 3 and 4a). The result indicates that fault density in the hanging-wall block is larger than in the footwall (Fig. 8a). To the south, closer to Zone 2 (Fig. 3), fault density is similar on both blocks, with fault density approaching a number of 12 faults/km (Fig. 8a). On the footwall block of BF1 fault density decreases to the north, revealing a denser fault distribution closer to Zone 2. Figure 8b shows fault density in Zones 1 and 3; the data showing that fault density in Zone 1 (8-12 faults/km) is larger than fault density in Zone 3 (6-8 faults/km).

5.2 Geometry of the accommodation zone

The accommodation zone separating faults in Zones 1 and 3 is described following the definition in Faulds and Varga (1998). To these authors, accommodation zones comprise belts of overlapping fault terminations that separate either systems of uniformly dipping normal faults or adjacent domains of opposite-dipping normal faults. In the study area, the strike direction of an interpreted accommodation zone is near-perpendicular to the overall strike direction of the normal faults that terminate into it (Fig. 3).

The strike direction of this transverse accommodation zone (TAZ) is E-W. The TAZ is approximately 4500 m-long and 200 m-wide, with numerous opposite-dipping faults terminating or propagating into it (Figs. 3 and 4c). The TAZ was formed in association with the growth of two opposite-dipping fault families in Zones 1 and 3. With continuing lateral fault propagation in both Zone 1 and Zone 3, the transverse accommodation zone narrows.

6. Evidence of fault growth, reactivation and segment linkage

Throw vs. depth (T-Z) plots and throw vs. distance (T-D) plots are used in this section to analyse the growth history of the faults (Baudon and Cartwright, 2008a,b; Durogbitan, 2016). Non-reactivated faults are generally characterised by M-type or C-type throw-depth profiles, with throws tipping out towards the lower tip without a clear detachment (Baudon and Cartwright, 2008b). Reactivated faults exhibit stepped vertical throw-depth profiles (double C throw profile with one episode of reactivation) and their lower parts show a similar throw profile to non-reactivated faults. Fault reactivation modes are divided into upward reactivation and dip-linkage reactivation (Baudon and Cartwright, 2008b). However, crestal faults are usually with small throw values (Morley, 2007), which make it difficult to differentiate between these two modes. In this paper, reactivation is referred both to upward and dip-linkage reactivation. Fault segmentation is analysed with throw-distance profiles. Faults that show only one fault segment often present a maximum throw value at their centre, diminishing towards both tips (Lohr et al., 2008; Mansfield and Cartwright, 2001). Faults that are formed by lateral linkage of different segments often present several peak values in throw, with lower throw values at the linkage area (Walsh et al., 2003).

6.1 Group 1 faults

Group 1 comprises a set of faults with the largest displacements on the salt ridge (Fig. 4). A few of these Group 1 faults are still active and propagate onto the seafloor (Figs. 4, 5 and 6). Faults 1A to 1D in Zone 1, and 1E to 1H in Zone 3, were analysed in terms of their growth history (Fig. 9, see Figs. 3 and 4 for their locations), with fault 1A comprising border fault 1 (BF1) in Zone 1 and faults 1E (BF3) and 1G (BF4) comprising border faults in Zone 3.

Faults 1A and 1B in Zone 1 are interpreted to form two hard-linked fault segments, whereas fault 1C and 1D comprise single fault segment (Fig. 9). The reactivation history of faults in Zone 1 is constrained by Horizon H3 and H5, which are two main erosional surfaces identified on top of the salt diapir (Fig. 4). Profiles 1B-e show typical examples of fault reactivation bounded by horizons H3 and H5 (Fig. 9). Note that profiles 1B-e, 1B-f, 1C-h, 1C-i and 1D-j clearly show a first episode of fault reactivation in Zone 1, which is marked by Horizon H3, with only one exception in 1B-d where fault reactivation happened earlier. The second episode of reactivation in Group 1 faults (Zone 1) is marked by Horizon H5, as shown in profiles 1A-b, 1A-c and 1B-e. The T-Z plots for 1B-d and 1D-k indicate that this second episode fault reactivation occurred slightly earlier than H5, whereas 1B-g and 1D-j show that fault reactivation happened after H5 (Fig.9).

Faults 1E and 1H in Zone 3 are interpreted to comprise a single fault segment, with fault 1F and 1G comprising two fault segments (Fig. 9). Similar to Zone 1, fault reactivation of Group 1 faults in Zone 3 also shows two distinct episodes marked by H3 and H5 (Fig. 9). The first episode of fault reactivation in Zone 3 is revealed by the T-Z plots of 1E-b, 1G-j, 1G-k and 1H-l to 1H-n (Fig. 9). The second episode of fault reactivation, marked by horizon H5, affected the T-Z profiles in 1E-b, 1E-c, 1F-d, 1F-e, 1G-1 to 1G-i, 1H-m and 1H-n.

Even though two episodes of fault reactivation are identified in both Zone 1 and 3, not all faults record two episodes of fault reactivation. Exceptions are fault 1C in Zone 1 and faults 1F and 1G in Zone 3, which reveal one single episode of fault reactivation.

Maximum throw values of Group 1 faults vary from 30 to 80 ms TWT, with border faults 1A, 1E and 1G reaching a maximum of 80 ms TWT. Away from the border faults, maximum throw value can reach a maximum of 40 ms TWT in other Group 1 faults (Fig. 9).

6.2 Group 2 faults

Faults interpreted as part of Group 2 are named 2A to 2D in Zone 1, and 2E to 2H in Zone 3 (Fig. 10, see Figs. 3 and 5 for their location).

Fault 2A, also referred as Border Fault 2, has a maximum throw value of ~60 ms TWT (Fig. 10). Except for this latter, faults in Zone 1 comprise two fault segments, with fault 1A showing one single fault segment. Fault reactivation of Group 2 faults occurs around Horizon H3 (Fig. 10). However, this group of faults indicates a complicated reactivation history. Profiles 2B-e to 2B-g and fault 2C-j reveal two episodes of fault reactivation (Fig. 10). Profiles 2B-d, 2C-h and 2D-k are 'C' type faults on T-Z data, a character indicating the absence of reactivation. An important aspect is that faults 2C and 2D comprise two fault segments of distinct length (Fig. 10), with the shorter fault segment showing a non-reactivated T-Z profile (profile 2C-h of fault 2C and profile 2D-k of fault 2D). Conversely, the longer fault segment reveals fault reactivation. Fault 2B, which comprises two comparable fault segments, also shows a non-reactivated fault segment (profile 2B-d) and a reactivated one (2B-e to 2B-g) (Fig. 3).

Group 2 faults in Zone 3 comprise two fault segments except for fault 2H, which is interpreted to form one single segment (Fig. 10). Fault reactivation history in Zone 3 also occurred around Horizon H3. T-Z plots generally indicate one episode of fault reactivation, with exceptions in profiles 2E-a, 2G-h and 2G-i (non-reactivated) and profile 2E-j with two episodes of fault reactivation (Fig. 10). Similar to faults 2B to 2D in Zone 1, fault 2E and fault 2G also indicate that one fault segment is reactivated while the other is not (Fig.10).

Except for fault 2A, maximum throw values for Group 2 faults vary from 30 to 40 ms TWT, values that are far greater than the maximum throw of faults in Groups 3 (12 to 15 ms TWT) and 4 (4 to 8 ms TWT).

6.3 Group 3 faults

Faults named 3A to 3D (Zone 1) and 3E to 3H (Zone 3) comprise Group 3 faults (Fig. 11). In Zone 1, faults 3A, 3C and 3D comprise two hard-linked fault segments and fault 3B comprises three fault segments (Fig. 11). In Zone 3, faults 3F and 3H are interpreted to be single fault segment, fault 3E has two hard-linked fault segments, and fault 3G comprises four linked fault segments (Fig. 11).

One single episode of fault reactivation is recognised in Group 3. In Zone 1, fault reactivation is recorded at Horizon 3 (Profiles 3A-a, 3D-h and 3D-i). However, fault profiles 3A-b 3B-d and 3C-f indicate an earlier episode of fault reactivation. In Zone 3, the reactivation happened earlier than Horizon H3 (profiles 3E-a, 3F-c, 3H-g and 3H-h).

Similar to faults 2B to 2E, and fault 2G in Group 2, faults 3B, 3C, 3E, 3F and fault 3G in Group 3 comprise at least two fault segments with distinct reactivation histories (Fig. 11). Some of these segments show no reactivation. Maximum throw values for Group 3 vary from 12 ms to 15 ms TWT, a value larger than the maximum throw of Group 4 faults (Fig. 11).

6.4 Group 4 (non-reactivated) faults

Group 4 faults are restricted to Zone 1 (Fig. 4a). Four distinct faults named 4A to 4D were analysed through the compilation of T-Z plots (Fig. 12a-h) and by measuring absolute throw values along horizon H3 (Fig. 12). This group of faults were not reactivated, with maximum throws showing relatively small values between 4 ms and 8 ms TWT (Fig. 12). These values are within the resolution limits of seismic data, which was processed with sampling rate of 2 ms. Throw-depth (T-Z) plots for this group of faults show typical 'C' shape profiles (Baudon and Cartwright, 2008a). The upper tips of these faults are eroded away at Horizon H3 (Fig. 12). Throw-Length profiles for fault 4D show a single throw peak, suggesting the development of a single fault segment. Throw-length profiles for faults 4A, 4B and 4C show asymmetrical "M" shapes, which reflect the linkage of two distinct fault segments.

7. Geometry of crestal faults in time and space

Crestal fault families are often hard to document on seismic data or at outcrop (Randles et al., 2012). Nevertheless, Alves (2012) proposed that gravitational gliding contributes to the formation and evolution of crestal fault families. In addition, Yin and Groshong (2007) recognised that the evolution history of crestal fault families is controlled by master fault(s), here we refer as border fault(s). According to the latter authors, master faults are initiated during early stages of faulting and are capable of developing a more complicated fault pattern. Some other common characteristics of crestal faults include: a) their relatively small length, which normally does not exceed 2.3 km (Alves, 2012), and b) their relatively small throws, often below 50 ms TWT (Morley, 2007).

A second key characteristic, implying that fault throw is below 50 ms TWT, is not followed by the border faults in this study (see Randles et al., 2012). Four border faults are identified in the study area; faults 1A and 2A in Zone 1, and faults 1E and 1G in Zone 3 (Fig. 3). Without exception, all border faults show maximum throw of ~80 ms TWT (Figs. 9 and 10). This distinct throw distribution confirms that most of the stress and strain on the crest of the interpreted salt ridge has been accommodated by border faults. Fault density of the crestal fault system in Espírito Santo Basin varies from 4 to 8 per km on the footwall of the border faults, to 10-18 per km on their hanging-wall block (Fig. 8a), which implies that border faults might have hindered fault growth farther from the salt edge (Fig. 3). Comparing fault density in Zones 1 and 3, Zone 3 has a higher fault density than that in Zone 1 (Fig. 8b), which might reflect distinct fault-initiation processes.

The analysis of maximum throw vs depth is an efficient way to identify the depth faults first nucleated (Alves, 2012). However, this method is used on the basis that space is available for faults to propagate both upward and downwards, and this method loses its practical meaning when faults sole into a detachment surface. In this case, faults are most likely to propagate upward, with maximum throw developing only in an upward direction. To avoid this caveat, Group 3 and Group 4 faults were selected to compile maximum throw vs. depth plots as these two groups of faults are not detached on the salt ridge (Fig. 4). Expansion index (EI), which is the ratio between the thickness of hanging-wall and footwall strata (Lewis et al., 2013; Mansfield and Cartwright, 1996), was used to identify periods of significant fault growth. When EI >1, representing hanging-wall thickening, active fault growth occurs (Omosanya et al., 2015). In this paper, we selected border faults (faults 1A and 2A in Zone 1, faults 1E and 1G in Zone 3), which are still active, to calculate their expansion index and to estimate relative timing of fault growth episodes.

The maximum throw vs. depth plot in Figure 13 shows that faults in both Zone 1 and Zone 3 are nucleated within Unit 1 to Unit 3, with maximum throw located within Unit 2. The nucleation of faults reveals that faults in both Zone 1 and Zone 3 were formed during the middle-late Eocene, when the Abrolhos Bank was being formed and volcaniclastics were transported into Espírito Santo Basin inducing local halokinesis (Fiduk et al., 2004). Comparing the relative depth of maximum fault throws in Zones 1 and 3, it becomes obvious that faults in Zone 3 (Fig. 3) were formed before faults in Zone 1, and present relatively deeper maximum throw locations (Fig. 13).

Expansion indexes of border faults in Zones 1 and 3 (Fig. 14) also indicate that faults in Zone 3 formed earlier than faults in Zone 1. The first growth episode in Zone 1 occurred between H2-1 and H2-2, with expansion indexes above 1.0. In Zone 3, the first episode of fault growth occurred between H2 and H2-1 i.e., earlier than the first episode of fault growth in Zone 1. Combining maximum throw values vs. depth and expansion index data for border faults in Zones 1 and 3, we conclude that faults in Zone 3 formed earlier than their counterparts in Zone 1.

8. Discussion

8.1 Controlling factors on fault reactivation offshore Espírito Santo

The growth of faults is often controlled by reactivated basement structures (Pinheiro and Holdsworth, 1997). Bellahsen and Daniel (2005) later suggested that the relationship between the orientation of existing faults and the orientation of stresses to be key parameters leading to fault growth and reactivation. If the strike direction of existing faults and the orientation of principle stress are in a favourable relationship, faults are easier to grow and reactivate

(Baudon and Cartwright, 2008b). In the study area, the main strike direction of faults varies from NW to NE (Fig. 3). Except for faults 3B, 2B, 3A, 4B, 3C, 4C, which show a concentric pattern (Fig. 3), crestal faults strike N-S to NNE in the study area, a direction matching positively with the overall direction of extension for the South Atlantic margin (Chang et al., 1992; Petri, 1987), and with the regional stresses recorded on the margin at present (Heidbach et al., 2008). However, extension alone cannot justify the recorded variations in the strike of the interpreted crestal faults as local stresses on the flanks of salt structures change sharply in space and time, influencing fault growth (Hubbert and Rubey, 1959; Jain et al., 2013; Wiprut and Zoback, 2000). In addition, known factors influencing fault growth and reactivation around salt structures include salt dissolution (Randles et al., 2012) and multi-phase salt growth, both potentially associated with fault reactivation in the study area. Faults that show a concentric pattern (faults 3B, 2B, 3A, 4B, 3C, 4C; see Fig. 3 for the location) reflect salt withdrawal beneath the central depression generated on the salt ridge (Ge and Jackson, 1998; Ward et al., 2016).

In this study, we propose that border faults accommodated regional E-W extensional stresses recorded offshore Espírito Santo (Chang et al., 1992; Jacques, 2003). The growth of faults in the study area follows two distinct stages. Stage 1 records the growth of border faults, followed later by collapse of the salt ridge in distinct styles. In such a setting, crestal faults closer to border faults were harder to initiate and grow than those further away (Fig. 15). Border fault 1 was reactivated during a second episode of fault reactivation, which is marked by horizon H5 (Fig. 9). Throw-depth (T-Z) data for BF1 (Fig. 9) indicates that fault throw reaches a minimum value around H3, with a second peak in throw recorded after the second erosion phase is identified on the crest of the salt ridge (H5 in Figs. 4a and 5). This suggests that border faults kept accommodating strain and stress on the crest of the salt ridge - once crestal faults were far enough from border faults, they tended to grow and reactivate (Fig. 15).

In Zone 1, faults surrounding BF1 and BF2 chiefly comprise faults in Groups 2 and 3 (Fig. 3), which have far smaller displacement and length and a simpler reactivation history than the border faults (Figs. 9-12). Noting that faults closer to BF2 belong to Group 3 (Fig. 3), farther to the east Group 2 faults were firstly dominant before the generation of BF1. In Zone 3, in both sides of fault 1E, maximum fault throws tend to decrease ($T_{max2F} > T_{max2E} > T_{max3F}$ to the west and $T_{max1F} > T_{max2G} > T_{max2H}$ to the East) (Figs. 9 and 10).

The propagation history of the interpreted fault families does not agree with the 'coherent model' of Jackson and Rotevatn (2013), as faults commonly comprise two or more linked segments (Giba et al., 2012; Morley, 1999; Walsh et al., 2003; Walsh et al., 2002a) (Figs. 9 to 12). In the 'coherent model' of Jackson and Rotevatn (2013), faults have similar length and throw profiles and are linked early in their development to form large segments. This work proposes that larger fault segments in the study area propagated and were reactivated to link with smaller fault segments, and then evolved together as a set of related structures (Fig. 16). The larger, mature faults result from the linkage of several fault segments, and this mode is here identified as the predominant mode of lateral fault propagation in the study area (Figs. 9 to 12). The generation of larger faults is thus interpreted to have been controlled by several small existing fault segments, rather than by a large fault generated at the start of fault propagation (Sibson, 1985).

Throw-depth (T-Z) plots have been assessed for their accuracy as a method to identify fault growth and reactivation. In particular Lohr et al. (2008) pointed out that in listric faults, especially those in areas of important salt tectonics, throw values can approach zero and their practical meaning is quantitatively lost. However, in most published cases, throw is a reliable proxy for fault development and reactivation episodes. Even though the T-Z plots in time domain compiled in this study show well-expressed fault reactivation histories (Figs. 9-11), difficulties still exist when interpreting these T-Z plots. In the study area, throw values for crestal faults are less than 80 ms TWT (generally <50ms TWT), causing some difficulties in interpreting fault reactivation with accuracy. However, fault reactivation episodes are better constrained when using two erosional surfaces as temporal markers, H3 and H5. Thus, we suggest erosional surfaces as markers for identifying fault reactivation on the crest of salt structures. In combination with T-Z plots, interpreters can have a better evaluation of fault reactivation history by using key stratigraphic markers. In the studied crestal fault system, H3 and H5 are recognised as key markers to assess fault reactivation (Figs. 9 to 12). These two erosional surfaces also mark the boundaries above which faults were not reactivated; for instance, not all faults offset H3 or H5 (Fig. 4). Fault 2A (Fig. 10) is a good example, as this fault offsets H3 and stops at H5, with no further evidence of reactivation above this latter stratigraphic marker.

As a corollary of our analysis, fault propagation above the interpreted salt ridge is more complex than documented by Baudon and Cartwright (2008b) on other salt structures of the Espírito Santo Basin. The three-stage model of fault growth proposed by these latter authors is thus expanded in this work into a five-stage model (Fig. 17). The T-Z profiles of faults 1A (a), 1B (d and e), 1D (j and k), 1E (b) and 1H (m and n) (Fig. 11) exemplify this five-stage fault growth model. See for T-Z profile j of fault 1D for example; fault throw shows a first peak around 3100 ms TWT, while the second growth phase is indicated with a small peak at H5. A third growth episode is marked with increasing throw close to the seafloor (Fig. 9).

8.2 Importance of accommodation zones on the crest of salt structures

Numerous studies have been carried out to understand the formation of accommodation zones (Bosworth, 1985; Colletta et al., 1988; Langhi and Borel, 2008; Tesfaye et al., 2008). Fault systems that form accommodation zones in rifts are genetically related faults formed at approximately the same time (Coffield, 1987; Ebinger, 1989; Farhoud, 2009; Faulds et al., 1990; Kong et al., 2005). In the study area, the northern fault system (Zone 1) created multiple E-dipping faults that dip in an opposite direction to faults in Zone 3, with an E-trending accommodation zone separating these two zones (Fig. 3). Faults in Zones 1 and 3, however, reflect different formation mechanisms, with the northern fault system (Zone 1) showing geometries typical of collapse structures (Fig. 3), whereas the southern fault system (Zone 3) resembles faults formed by gravitational gliding (Fig. 4b) during withdrawal of salt on top of the salt diapir (Fig. 3). The interpreted top salt does not match with these mechanisms as this salt diapir is in an uplifting episode (Fig. 4). The different mechanisms for the two opposite-dipping fault families hint at distinct timings for the formation of opposite dipping fault systems. The depth in which maximum throw is observed indicates that fault nucleation in Zone 3 happened earlier than in Zone 1 (Fig. 13). The expansion indexes of border faults in Zone 1 and Zone 3 also indicate that the southern gravitational fault array formed slightly earlier than the northern collapsed fault array (Fig. 14). In Zone 1, the concentric faults observed are likely associated with the dissolution (and quick) collapse of salt underneath the post-salt overburden, which shows significant throw values for BF1 on top of the salt surface (Fig. 4a). Zone 3, in contrast, shows the predominance of gravitational gliding over the interpreted fault ridge. For instance, in Figure 4b the uniformly west-dipping fault array shows a continuous and smooth salt surface and some of the faults detach on the top of the salt; no significant faults intersect the top of the salt package (Fig. 4b). Also fault density in Zone 1 is higher, which indicates a predisposition for fault initiation in Zone 1. Despite these distinct mechanisms, faults in Zones 1 and 3 are kinematically linked and resulted in the generation of the TAZ in Zone 2. The distinct mechanisms observed (gliding vs. dissolution) resulted in locally focused, changing styles of crestal faulting.

Figure 18 illustrates the formation of the TAZ. Few faults formed by gravitational gliding in Zone 3 in a first stage due to gradual salt-withdrawal and generation of the depression on top of the salt ridge (Fig. 3). The sudden collapse of the ridge crest resulted in the formation of two opposite-dipping fault families in Stage 2. Further propagation of the faults in Zones 1 and 3 resulted in the formation of the TAZ, and faults stopped propagating horizontally across the accommodation zone (Figs. 18 and 19). However, this did not hinder later stages of vertical propagation in the interpreted faults, with structures oriented favourably for reactivation revealing blind vertical propagation towards the surface. This characteristic is again shown in Fig. 4, in which most of the faults are still active and propagate to the present seafloor.

9. Conclusions

High resolution seismic data from the Espírito Santo Basin, SE Brazil, documents a swarm of fault systems families on a salt ridge. Detailed mapping, throw-depth plots and statistical analyses of fault distributions provided us with important insights into the geometry and evolution of crestal fault systems of salt structures. This work resulted in the following conclusions:

1) A swarm of listric, moderately–highly curved and faults are developed on top of the salt ridge, showing seismic resolved fault densities that can reach as much as eighteen (18) faults/km.

2) The crestal fault family is controlled by listric border faults i.e., border faults have larger maximum throws than the remainder of crestal faults and accommodate most the strain and stress on the crest of the salt structure. At the same time, other crestal faults formed close

to border faults are less active. Border faults are also in a preferential position to be reactivated.

3) Erosional surfaces are robust markers to date fault reactivation, particularly when used together with T-Z plots.

4) Segment linkage is predominant within the interpreted crestal fault families and controlled fault growth. The interpreted crestal faults propagated both vertically and horizontally. Over the salt ridge, horizontal propagation was hindered by an accommodation zone, onto which faults terminate. Vertical propagation stops either the fault meets the seafloor or vertical propagation is accommodated by either blind faults, or by adjacent faults with larger displacement.

5) Fault propagation does not follow the 'Coherent model' of Jackson and Rotenvadt (2013). The geometry and history of propagation of faults segments are not comparable with this later model. In particular, large fault segments propagated to emerge with non-reactivated small fault segments on the crest of the salt ridge, and can show later blind propagation towards the surface.

6) The transverse accommodation zone (TAZ) developed on the salt ridge had paramount influence on the evolution of the interpreted crestal faults. Two opposite-dipping fault families, reflecting distinct mechanisms for their formation, terminate into the accommodation zone. After its establishment, the development of the crestal fault system became controlled by the accommodation zone.

Acknowledgements

We thank CGG for the permission to use the seismic data in this paper and Schlumberger for the provision of Petrel® for seismic interpretation. We acknowledge the contributions of Chris Morley, Paul Wilson, Marco Bonini and another anonymous reviewer that greatly improved the quality of the paper. Tao Ze also thanks the China Scholarship Council (CSC) for supporting the PhD project from which this work has derived. Tao Ze thanks his colleagues in the 3D Seismic Lab for the help and tips provided.

References

Alsop, G.I., Weinberger, R., Levi, T., Marco, S., 2015. Deformation within an exposed salt wall: Recumbent folding and extrusion of evaporites in the Dead Sea Basin. Journal of Structural Geology 70, 95-118.

Alves, T.M., 2012. Scale-relationships and geometry of normal faults reactivated during gravitational gliding of Albian rafts (Espírito Santo Basin, SE Brazil). Earth and Planetary Science Letters 331-332, 80-96.

Alves, T.M., Cartwright, J., Davies, R.J., 2009. Faulting of salt-withdrawal basins during early halokinesis: Effects on the Paleogene Rio Doce Canyon system (Espirito Santo Basin, Brazil). AAPG Bull. 93, 617-652.

Alves, T.M., Cartwright, J.A., 2009. Volume balance of a submarine landslide in the Espirito Santo Basin, offshore Brazil: Quantifying seafloor erosion, sediment accumulation and depletion. Earth and Planetary Science Letters 288, 572-580.

Baars, D., Stevenson, G., 1982. Subtle stratigraphic traps in Paleozoic rocks of Paradox basin. AAPG Memoir, 131 - 158.

Barnett, J.A., Mortimer, J., Rippon, J.H., Walsh, J.J., Watterson, J., 1987. Displacement geometry in the volume containing a single normal fault. AAPG Bull. 71, 925-937.

Baudon, C., Cartwright, J., 2008a. Early stage evolution of growth faults: 3D seismic insights from the Levant Basin, Eastern Mediterranean. Journal of Structural Geology 30, 888-898.

Baudon, C., Cartwright, J., 2008b. The kinematics of reactivation of normal faults using high resolution throw mapping. Journal of Structural Geology 30, 1072-1084.

Bellahsen, N., Daniel, J.M., 2005. Fault reactivation control on normal fault growth: an experimental study. Journal of Structural Geology 27, 769-780.

Bose, S., Mitra, S., 2010. Analog modeling of divergent and convergent transfer zones in listric normal fault systems. AAPG Bull. 94, 1425-1452.

Bosworth, W., 1985. Geometry of propagating continental rifts. Nature 316, 625-627.

Bruhn, C.H., Walker, R.G., 1997. Internal architecture and sedimentary evolution of coarse-grained, turbidite channel-levee complexes, Early Eocene Regencia Canyon, Espirito Santo Basin, Brazil. Sedimentology 44, 17-46.

Cainelli, C., Mohriak, W.U., 1999. General evolution of the eastern Brazilian continental margin. The Leading Edge 18, 800, 802-861.

Cartwright, J., 2011. Diagenetically induced shear failure of fine-grained sediments and the development of polygonal fault systems. Marine and Petroleum Geology 28, 1593-1610.

Cartwright, J., Huuse, M., Aplin, A., 2007. Seal bypass systems. AAPG Bull. 91, 1141-1166.

Cartwright, J., Trudgill, B., Mansfield, C., 2000. Fault growth by segment linkage: An explanation for scatter in maximum displacement and trace length data from the Canyonlands grabens of SE Utah: Reply. Journal of Structural Geology 22, 141-143.

Cartwright, J.A., Trudgill, B.D., Mansfield, C.S., 1995. Fault growth by segment linkage: an explanation for scatter in maximum displacement and trace length data from the Canyonlands Grabens of SE Utah. Journal of Structural Geology 17, 1319-1326.

Chang, H., Kowsmann, R., Defigueiredo, A., 1988. New concepts on the development of east Brazilian marginal basins. Episodes 11, 194-202.

Childs, C., Manzocchi, T., Walsh, J., Bonson, C.G., Nicol, A., Schopfer, M., 2009. A geometric model of fault zone and fault rock thickness variations. J. Struct. Geol. 31, 117-127.

Chopra, S., Marfurt, K., 2007. Curvature attribute applications to 3D surface seismic data. The Leading Edge 26, 404-414.

Clausen, O.R., Egholm, D.L., Andresen, K.J., Wesenberg, R., 2014. Fault patterns within sediment layers overlying rising salt structures: A numerical modelling approach. Journal of Structural Geology 58, 69-78.

Coffield, D.Q., 1987. Surface expression and internal structure of an accommodation zone, Gulf of Suez, Egypt. Aapg Bulletin-American Association of Petroleum Geologists 71, 540-540.

Colletta, B., Le Quellec, P., Letouzey, J., Moretti, I., 1988. Longitudinal evolution of the Suez rift structure (Egypt). Tectonophysics 153, 221-233.

Cowie, P., Gupta, S., Dawers, N., 2000. Implications of fault array evolution for synrift depocentre development: insights from a numerical fault growth model. Basin Research 12, 241-261.

Cowie, P.A., Scholz, C.H., 1992. Physical explanation for the displacement-length relationship of faults using a post-yield fracture mechanics model. Journal of Structural Geology 14, 1133-1148.

Crossley, R., Crow, M., 1980. The Malawi rift. Geodynamic Evolution of the Afro-Arabian rift system, 78-87.

Davison, I., 2007. Geology and tectonics of the South Atlantic Brazilian salt basins. Geological Society, London, Special Publications 272, 345-359.

Davison, I., Alsop, I., Birch, P., Elders, C., Evans, N., Nicholson, H., Rorison, P., Wade, D., Woodward, J., Young, M., 2000. Geometry and late-stage structural evolution of Central Graben salt diapirs, North Sea. Mar. Pet. Geol. 17, 499-522.

Demercian, S., Szatmari, P., Cobbold, P., 1993. Style and pattern of salt diapirs due to thin-skinned gravitational gliding, Campos and Santos basins, offshore Brazil. Tectonophysics 228, 393-433.

Durogbitan, A.A., 2016. Investigating fault propagation and segment linkage using throw distribution analysis within the Agbada formation of Ewan and Oloye fields, northwestern Niger delta. Journal of African Earth Sciences.

Ebinger, C.J., 1989. Geometric and kinematic development of border faults and accommodation zones, Kivu-Rusizi Rift, Africa. Tectonics 8, 117-133.

Ebinger, C.J., Rosendahl, B., Reynolds, D., 1987. Tectonic model of the Malaŵi rift, Africa. Tectonophysics 141, 215-235.

Farhoud, K., 2009. Accommodation zones and tectono-stratigraphy of the Gulf of Suez, Egypt: A contribution from aeromagnetic analysis. Geoarabia 14, 139-162.

Faulds, J.E., Geissman, J.W., Mawer, C.K., 1990. Structural development of a major extensional accommodation zone in the Basin and Range Province, northwestern Arizona and southern Nevada; Implications for kinematic models of continental extension. Geological Society of America Memoirs 176, 37-76.

Faulds, J.E., Varga, R.J., 1998. The role of accommodation zones and transfer zones in the regional segmentation of extended terranes. Special papers-Geological Society of America 323, 1-46.

Fiduk, J.C., Brush, E.R., Anderson, L.E., Gibbs, P.B., Rowan, M.G., 2004. Salt deformation, magmatism, and hydrocarbon prospectivity in the Espirito Santo Basin, offshore Brazil, Salt-sediment interactions and hydrocarbon prospectivity: Concepts, applications, and case studies for the 21st century: Proceedings of Gulf Coast Section SEPM Foundation Bob F. Perkins Research Conference. SEPM, pp. 370-392.

Fossen, H., Rotevatn, A., 2016. Fault linkage and relay structures in extensional settings—A review. Earth-Science Reviews 154, 14-28.

Furuya, M., Mueller, K., Wahr, J., 2007. Active salt tectonics in the Needles District, Canyonlands (Utah) as detected by interferometric synthetic aperture radar and point target analysis: 1992–2002. Journal of Geophysical Research: Solid Earth (1978–2012) 112.

Gamboa, D., Alves, T., Cartwright, J., Terrinha, P., 2010a. MTD distribution on a 'passive' continental margin: The Espirito Santo Basin (SE Brazil) during the Palaeogene. Marine and Petroleum Geology 27, 1311-1324.

Gamboa, D., Alves, T., Cartwright, J., Terrinha, P., 2010b. MTD distribution on a ‘passive’ continental margin: The Espírito Santo Basin (SE Brazil) during the Palaeogene. Marine and Petroleum Geology 27, 1311-1324.

Gamboa, D., Alves, T.M., 2015. Spatial and dimensional relationships of submarine slope architectural elements: A seismic-scale analysis from the Espírito Santo Basin (SE Brazil). Marine and Petroleum Geology 64, 43-57.

Garcia, S.F.D., Letouzey, J., Rudkiewicz, J.L., Danderfer, A., de Lamotte, D.F., 2012. Structural modeling based on sequential restoration of gravitational salt deformation in the Santos Basin (Brazil). Mar. Pet. Geol. 35, 337-353.

Gay, A., Lopez, M., Berndt, C., Seranne, M., 2007. Geological controls on focused fluid flow associated with seafloor seeps in the Lower Congo Basin. Marine Geology 244, 68-92.

Ge, H., Jackson, M.P., 1998. Physical modeling of structures formed by salt withdrawal: Implications for deformation caused by salt dissolution. AAPG Bull. 82, 228-250.

Gee, M., Gawthorpe, R., 2006. Submarine channels controlled by salt tectonics: Examples from 3D seismic data offshore Angola. Marine and Petroleum Geology 23, 443-458.

Giba, M., Walsh, J.J., Nicol, A., 2012. Segmentation and growth of an obliquely reactivated normal fault. Journal of Structural Geology 39, 253-267.

Gutiérrez, F., 2004. Origin of the salt valleys in the Canyonlands section of the Colorado Plateau: Evaporite-dissolution collapse versus tectonic subsidence. Geomorphology 57, 423-435.

Heidbach, O., Tingay, M., Barth, A., Reinecker, J., Kurfeß, D., Müller, B., 2008. The world stress map database release 2008, doi: 10.1594/GFZ. WSM. Rel2008.

Holdsworth, R., Butler, C., Roberts, A., 1997. The recognition of reactivation during continental deformation. Journal of the Geological Society 154, 73-78.

Hubbert, M.K., Rubey, W.W., 1959. Role of fluid pressure in mechanics of overthrust faulting I. Mechanics of fluid-filled porous solids and its application to overthrust faulting. Geological Society of America Bulletin 70, 115-166.

Hung Kiang Chang, R.O., Kowsmann, A., Bender, A.M.F., Figueiredo, A.M.F., 1992. Tectonics and stratigraphy of the East Brazil Rift system: an overview. Tectonophysics 213, 97-138.

Jackson, C.A.L., Larsen, E., 2009. Temporal and spatial development of a gravity-driven normal fault array: Middle–Upper Jurassic, South Viking Graben, northern North Sea. Journal of Structural Geology 31, 388-402.

Jackson, C.A.L., Rotevatn, A., 2013. 3D seismic analysis of the structure and evolution of a salt-influenced normal fault zone: A test of competing fault growth models. Journal of Structural Geology 54, 215-234.

Jacques, J.M., 2003. A tectonostratigraphic synthesis of the Sub-Andean basins: inferences on the position of South American intraplate accommodation zones and their control on South Atlantic opening. Journal of the Geological Society 160, 703-717.

Jain, A., Verma, A., Vishal, V., Singh, T., 2013. Numerical simulation of fault reactivation phenomenon. Arab. J. Geosci. 6, 3293-3302.

Jenyon, M.K., 1988. Overburden deformation related to the pre-piercement development of salt structures in the North-Sea. Journal of the Geological Society 145, 445-454.

Jung, N., Han, W., Watson, Z., Graham, J.P., Kim, K., 2014. Fault-controlled CO2 leakage from natural reservoirs in the Colorado Plateau, East-Central Utah. Earth Planet. Sci. Lett. 403, 358-367.

Kong, D.Y., Shen, H., Liu, J.Y., Yin, W., 2005. Origin of the transverse accommodation zone of the Shulu subbasin in the Jizhong depression. Geology in China 32, 694-695.

Langhi, L., Borel, G.D., 2008. Reverse structures in accommodation zone and early compartmentalization of extensional system, Laminaria High (NW shelf, Australia). Marine and Petroleum Geology 25, 791-803.

Lewis, M.M., Jackson, C.A.L., Gawthorpe, R.L., 2013. Salt-influenced normal fault growth and forced folding: The Stavanger Fault System, North Sea. Journal of Structural Geology 54, 156-173.

Leyden, R., Bryan, G., Ewing, M., 1972. Geophysical reconnaissance on African shelf: 2. Margin sediments from Gulf of Guinea to Walvis Ridge. AAPG Bull. 56, 682-693.

Lisle, R.J., Srivastava, D.C., 2004. Test of the frictional reactivation theory for faults and validity of fault-slip analysis. Geology 32, 569-572.

Liu, E., Wang, H., Li, Y., Leonard, N.D., Feng, Y., Pan, S., Xia, C., 2015. Relative role of accommodation zones in controlling stratal architectural variability and facies distribution: Insights from the Fushan Depression, South China Sea. Marine and Petroleum Geology 68, Part A, 219-239.

Lohr, T., Krawczyk, C.M., Oncken, O., Tanner, D.C., 2008. Evolution of a fault surface from 3D attribute analysis and displacement measurements. Journal of Structural Geology 30, 690-700.

Mansfield, C., Cartwright, J., 2001. Fault growth by linkage: Observations and implications from analogue models. Journal of Structural Geology 23, 745-763.

Mansfield, C.S., Cartwright, J.A., 1996. High resolution fault displacement mapping from three-dimensional seismic data: evidence for dip linkage during fault growth. Journal of Structural Geology 18, 249-263.

McLeod, A.E., Dawers, N.H., Underhill, J.R., 2000. The propagation and linkage of normal faults: insights from the Strathspey-Brent-Statfjord fault array, northern North Sea. Basin Res. 12, 263-284.

Mohriak, W., Nemcok, M., Enciso, G., 2008. South Atlantic divergent margin evolution: rift-border uplift and salt tectonics in the basins of SE Brazil. Geological Society, London, Special Publications 294, 365-398.

Mohriak, W.U., Szatmari, P., Anjos, S., 2012. Salt: geology and tectonics of selected Brazilian basins in their global context. Geological Society, London, Special Publications 363, 131-158.

Morley, C., Nelson, R., Patton, T., Munn, S., 1990. Transfer zones in the East African rift system and their relevance to hydrocarbon exploration in rifts (1). AAPG Bull. 74, 1234-1253.

Morley, C.K., 1999. Patterns of displacement along large normal faults: implications for basin evolution and fault propagation, based on examples from east Africa. AAPG Bull. 83, 613-634.

Morley, C.K., 2007. Development of crestal normal faults associated with deepwater fold growth. Journal of Structural Geology 29, 1148-1163.

Ojeda, H., 1982. Structural framework, stratigraphy, and evolution of Brazilian marginal basins. AAPG Bull. 66, 732-749.

Omosanya, K.d.O., Alves, T.M., 2013. Ramps and flats of mass-transport deposits (MTDs) as markers of seafloor strain on the flanks of rising diapirs (Espírito Santo Basin, SE Brazil). Marine Geology 340, 82-97.

Omosanya, K.d.O., Alves, T.M., 2014. Mass-transport deposits controlling fault propagation, reactivation and structural decoupling on continental margins (Espírito Santo Basin, SE Brazil). Tectonophysics 628, 158-171.

Omosanya, K.O., Johansen, S.E., Harishidayat, D., 2015. Evolution and character of supra-salt faults in the Easternmost Hammerfest Basin, SW Barents Sea. Marine and Petroleum Geology 66, Part 4, 1013-1028.

Petri, S., 1987. Cretaceous paleogeographic maps of Brazil. Palaeogeography, Palaeoclimatology, Palaeoecology 59, 117-168.

Pinheiro, R., Holdsworth, R., 1997. Reactivation of Archaean strike-slip fault systems, Amazon region, Brazil. J. Geol. Soc. 154, 99-103.

Randles, T., Clarke, S., Richards, P., 2012. Development of Crestal Collapse Structures above Dissolving Salt Anticlines: Application to Seismic Interpretation within Salt-Controlled Basins, AAPG Annual Convention and Exhibition, Long Beach, California.

Rijks, E., Jauffred, J., 1991. Attribute extraction: An important application in any detailed 3-D interpretation study. The Leading Edge 10, 11-19.

Rouby, D., Guillocheau, F., Robin, C., Bouroullec, R., Raillard, S., Castelltort, S., Nalpas, T., 2003. Rates of deformation of an extensional growth fault/raft system (offshore Congo, West African margin) from combined accommodation measurements and 3-D restoration. Basin Research 15, 183-200.

Rowan, M.G., Jackson, M.P.A., Trudgill, B.D., 1999. Salt-related fault families and fault welds in the northern Gulf of Mexico. Aapg Bulletin-American Association of Petroleum Geologists 83, 1454-1484.

Rowan, M.G., Lawton, T.F., Giles, K.A., Ratliff, R.A., 2003. Near-salt deformation in La Popa basin, Mexico, and the northern Gulf of Mexico: A general model for passive diapirism. AAPG Bull. 87, 733-756.

Schlische, R.W., Withjack, M.O., 2009. Origin of fault domains and fault-domain boundaries (transfer zones and accommodation zones) in extensional provinces: Result of random nucleation and self-organized fault growth. Journal of Structural Geology 31, 910-925.

Sibson, R.H., 1985. A note on fault reactivation. Journal of Structural Geology 7, 751-754.

Smith, G.A., McIntosh, W., Kuhle, A.J., 2001. Sedimentologic and geomorphic evidence for seesaw subsidence of the Santo Domingo accommodation-zone basin, Rio Grande rift, New Mexico. Bulletin of the Geological Society of America 113, 561-574.

Stewart, S., Ruffell, A., Harvey, M., 1997. Relationship between basement-linked and gravity-driven fault systems in the UKCS salt basins. Marine and Petroleum Geology 14, 581-604.

Stolt, R.H., Benson, A.K., 1986. Seismic migration: Theory and practice. Pergamon.

Storvoll, V., Bjrlykke, K., Mondol, N.H., 2005. Velocity-depth trends in Mesozoic and Cenozoic sediments from the Norwegian Shelf. AAPG Bull. 89, 359-381.

Tesfaye, S., Rowan, M.G., Mueller, K., Trudgill, B.D., Harding, D.J., 2008. Relay and accommodation zones in the Dobe and Hanle grabens, central Afar, Ethiopia and Djibouti. Journal of the Geological Society 165, 535-547.

Van der Veer, E., 2013. Induced seismicity in CO2 storage systems; A modeling study into the effect of thermally-induced stress changes on fault reactivation.

Vendeville, B.C., 2005. Salt tectonics driven by sediment progradation: Part I—Mechanics and kinematics. AAPG Bull. 89, 1071-1079.

Vendeville, B.C., Jackson, M.P.A., 1992a. The fall of diapirs during thin-skinned extension. Marine and Petroleum Geology 9, 354-371.

Vendeville, B.C., Jackson, M.P.A., 1992b. The rise of diapirs during thin-skinned extension. Marine and Petroleum Geology 9, 331-354.

Walsh, J., Bailey, W., Childs, C., Nicol, A., Bonson, C., 2003. Formation of segmented normal faults: a 3-D perspective. Journal of Structural Geology 25, 1251-1262.

Walsh, J., Nicol, A., Childs, C., 2002a. An alternative model for the growth of faults. Journal of Structural Geology 24, 1669-1675.

Walsh, J., Nicol, A., Childs, C., 2002b. An alternative model for the growth of faults. J. Struct. Geol. 24, 1669-1675.

Ward, N.I., Alves, T.M., Blenkinsop, T.G., 2016. Reservoir leakage along concentric faults in the Southern North Sea: Implications for the deployment of CCS and EOR techniques. Tectonophysics.

Wiprut, D., Zoback, M.D., 2000. Fault reactivation and fluid flow along a previously dormant normal fault in the northern North Sea. Geology 28, 595-598.

Yin, H., Groshong, R.H., 2007. A three-dimensional kinematic model for the deformation above an active diapir. AAPG Bull. 91, 343-363.

Figure captions

Figure 1 Regional maps of Southeast Brazilian margin showing: a) the relative location of the Southeast Atlantic margin. b) The location of the study area (red box). The dotted line indicates the limit of Aptian evaporites and the solid line shows the bathymetry (m). c) Variance map (Z=-3140ms TWT) of the study area. The red box indicates the location of the studied crestal fault system. d) Enlarged variance map of the studied fault system.

Figure 2 Simplified regional cross section of Espírito Santo Basin revealing major depositional sequences. Relative location of the study area is indicated by the black box (Modified from Fiduk et al., 2004 and Gamboa et al., 2010, 2011).

Figure 3 TWT structural map depicting the geometry of Opposite-Dipping Fault arrays (Zone 1 and Zone 3) and the Transverse Accommodation Zone (Zone 2) (TAZ). The area highlighted in the black box is the location of the studied ODF-TAZ system. The interpreted horizon is H3 (see also Fig. 4 and 6), the numbered faults are subsequently analysed (see Figs. 9-12). The interpreted area of horizon H3 is shown in Figure 1c.

Figure 4 Uninterpreted seismic sections and enlarged interpreted sections for Zones 1-3. a-b) Seismic sections of an E-dipping fault array with a few antithetic faults form graben-like structures (Zone 1). c-d) Seismic sections of a W-dipping fault array dipping uniformly to the west (Zone 3). e-f) Seismic sections across the transverse accommodation zone in which the two opposite dipping fault arrays interact (Zone 2). Locations of the seismic sections are shown in Figures 1d and 3. The different colours represent the four groups of faults considered in this study. Faults subsequently analysed are also labelled.

Figure 5 a) Main stratigraphic units on the crest of the interpreted salt ridge. Seven horizons are interpreted, with H1 representing the top surface of salt diapir and H7 representing the seafloor. b) Zoomed seismic section of the studied fault system. Location of the seismic section is shown in Figure 1d.

Figure 6 Seismic sections illustrating the four groups of faults (Group 1, Group 2, Group 3 and Group 4) interpreted on crest of the salt ridge. a) Un-interpreted seismic section, shown in Figure 1d. b) Interpreted seismic section. Faults offset H5 and some propagate towards the seafloor. Group 2 is bounded by H5 and offsets H4 – the top surface of Unit 2. Faults of Group 3 all form in Unit 2. Group 4 faults are limited to Unit 2.

Figure 7 Lower-hemisphere and equal-area projections of poles to fault planes show strike direction and dip angles of the crestal fault system. a) Average strike direction (354.74^0 NNW) and dip angle (35.37^0) of faults dipping to the east in Zone 1. b) Average strike direction (20.31^0 NNE) and dip angle (36.7^0) of faults dipping to the west in Zone 1. c) Average strike direction (5.34^0 NNE) and dip angle (35.94^0) of faults in Zone 3.

Figure 8 a) Statistical data for fault density on both hanging wall and footwall blocks of border fault 1 (Zone 1) as compiled from specific seismic sections in a south to north orientation. B) Fault density acquired on selected seismic sections in both Zones 1 and 3.

Figure 9 T-D and T-Z plots for Group 1 faults. Locations of Faults 1A to 1H are labelled in Figure 3. The vertical lines a-k in the T-D plots in row 1 and a-n in row 3 indicate the location of the T-Z plots in rows 2 and 4 respectively. Two episodes of fault reactivation are identified, which are marked by horizons H3 and H5.

Figure 10 T-D and T-Z plots for Group 2 faults. Locations of Faults 2A to 2H are labelled in Figure 3. The vertical lines a-m in the T-D plots in rows 1 and a-k in row 3 indicate the locations of the T-Z plots in rows 2 and 4 respectively. One episode of fault reactivation, marked by horizon H3, is recognised.

Figure 11 T-D and T-Z plots for Group 3 faults. Locations of Faults 3A to 3H are labelled in Figure 3. The vertical lines a-l in the T-D plots in row 1 and a-h in row 3 indicate the location of the T-Z plots in rows 2 and 4 respectively. Reactivation is recorded at horizon H3 in Zone 1. Reactivation in Zone 3 occurs earlier than H3.

Figure 12 T-D and T-Z plots of faults in Group 4. Locations of Faults 4A to 4D are labelled in Figure 3. The vertical lines a-h in the T-D plots in row 1 indicate the location of the T-Z plots in row 2. All the T-Z plots show a typical ‘C’ shape, which indicates that faults were not reactivated.

Figure 13 Maximum throw locations of Group 3 and 4 faults in Zone 1 and Group 3 faults in Zone 3 as tied to seismic stratigraphy units. The figure indicates that the formation of faults in Zone 3 is earlier than that of Zone 1.

Fig. 14 Expansion Indexes (EI) for the major faults showing variation in strata thickness across their hanging-wall and footwall blocks. An EI of >1 implies thickening of strata in the hanging-wall section, whereas EI < 1 means thinning relative to the footwall block.

Figure 15 Schematic illustration of the reactivation history of crestal faults in this study. Red boxes indicate zones of low fault reactivation close to the border faults. Blue boxes indicate zones of high reactivation away from the border faults.

Figure 16 Alternative “Isolated model” of fault propagation. Larger faults propagated and reactivated while small fault segments remain undisturbed until two fault segments are linked together. (1-2) map view; (3-4) T-D profile; (5-6) T-Z profile. The larger fault segment can be either reactivated or non-reactivated.

Figure 17 Schematic map showing throw-depth plots vs. repeated fault reactivation on crest of salt ridges. Each reactivation episode is associated with an erosional surface.

Figure 18 Plan-view of schematic map illustrates formation of a transverse accommodation zone. Stage 1 - Formation of a W-dipping fault array. Stage 2 - Crestal collapse, which was controlled by crestal faults creating multiple small-scale faults dipping to the east. West-dipping fault arrays kept propagating at this stage. Stage 3 - Late evolution stage of faults, with both fault systems intersecting each other to form an accommodation zone.

Figure 19 Schematic 3D panel showing the relationship between the transverse accommodation zone (TAZ) and crestal faults in the study area. The strike directions of the accommodation zone and faults are nearly perpendicular.

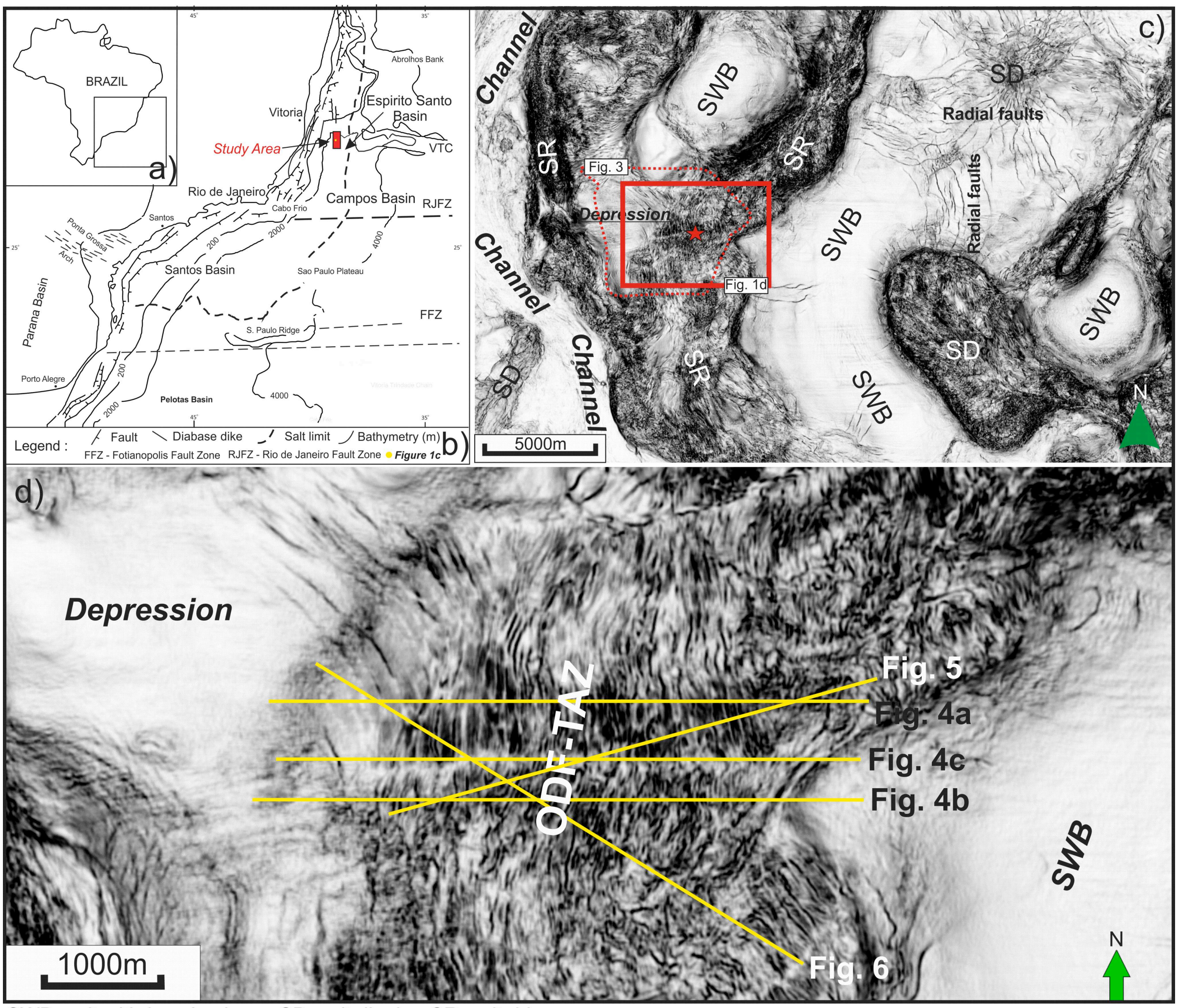

996 SWD: salt withdraw basins SD: salt diapir SR: salt ridge

997 Figure 1

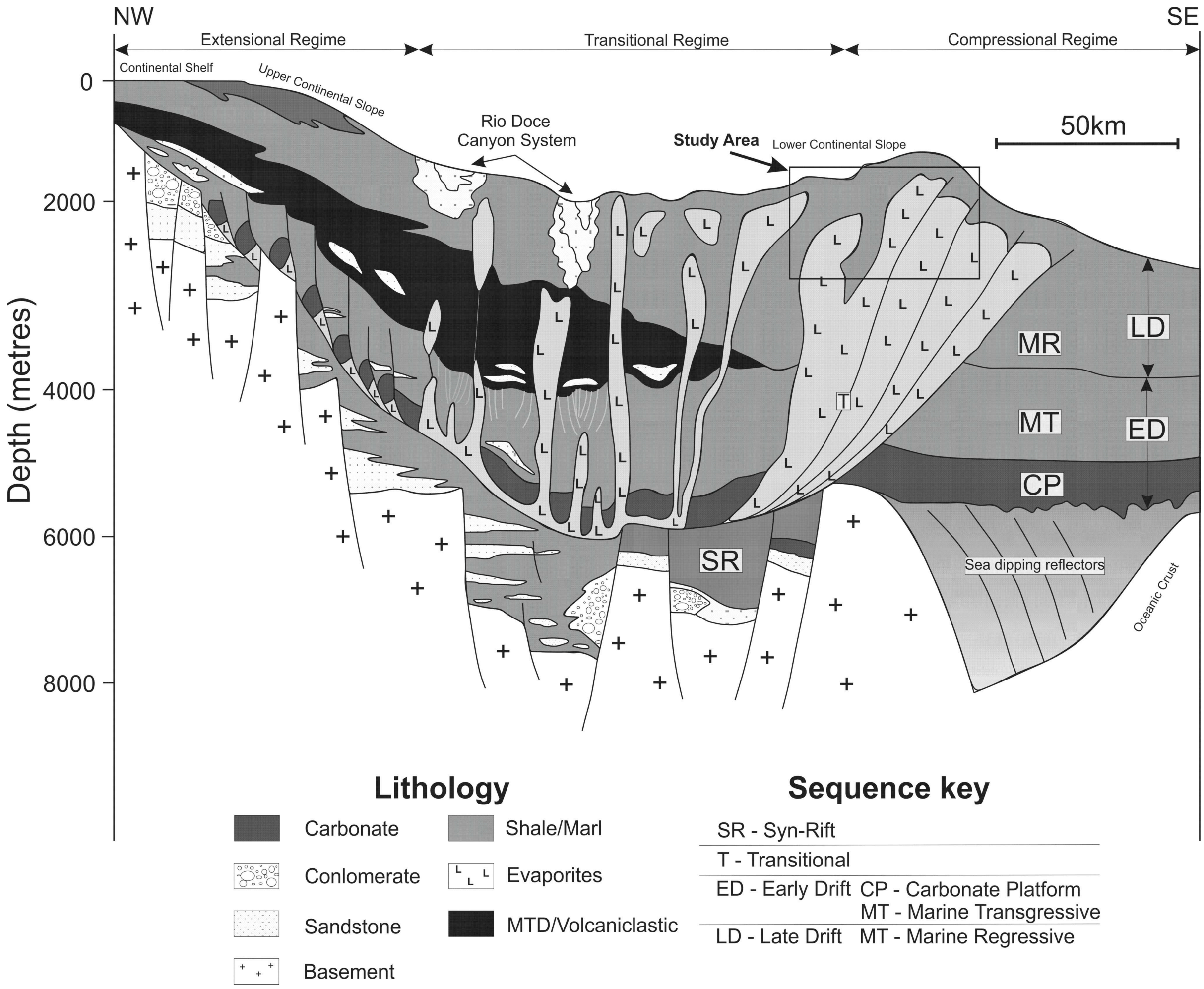

NW
SE
Extensional Regime
Transitional Regime
Compressional Regime
Continental Shelf
Upper Continental Slope
Rio Doce
Canyon System
Study Area
Lower Continental Slope
50km
0
2000
4000
6000
8000
Depth (metres)
MR
LD
MT
ED
CP
T
SR
Sea dipping reflectors
Oceanic Crust
Lithology
Carbonate
Shale/Marl
Conlomerate
Evaporites
Sandstone
MTD/Volcaniclastic
Basement
Sequence key
SR - Syn-Rift
T - Transitional
ED - Early Drift CP - Carbonate Platform
MT - Marine Transgressive
LD - Late Drift MT - Marine Regressive

Figure 2

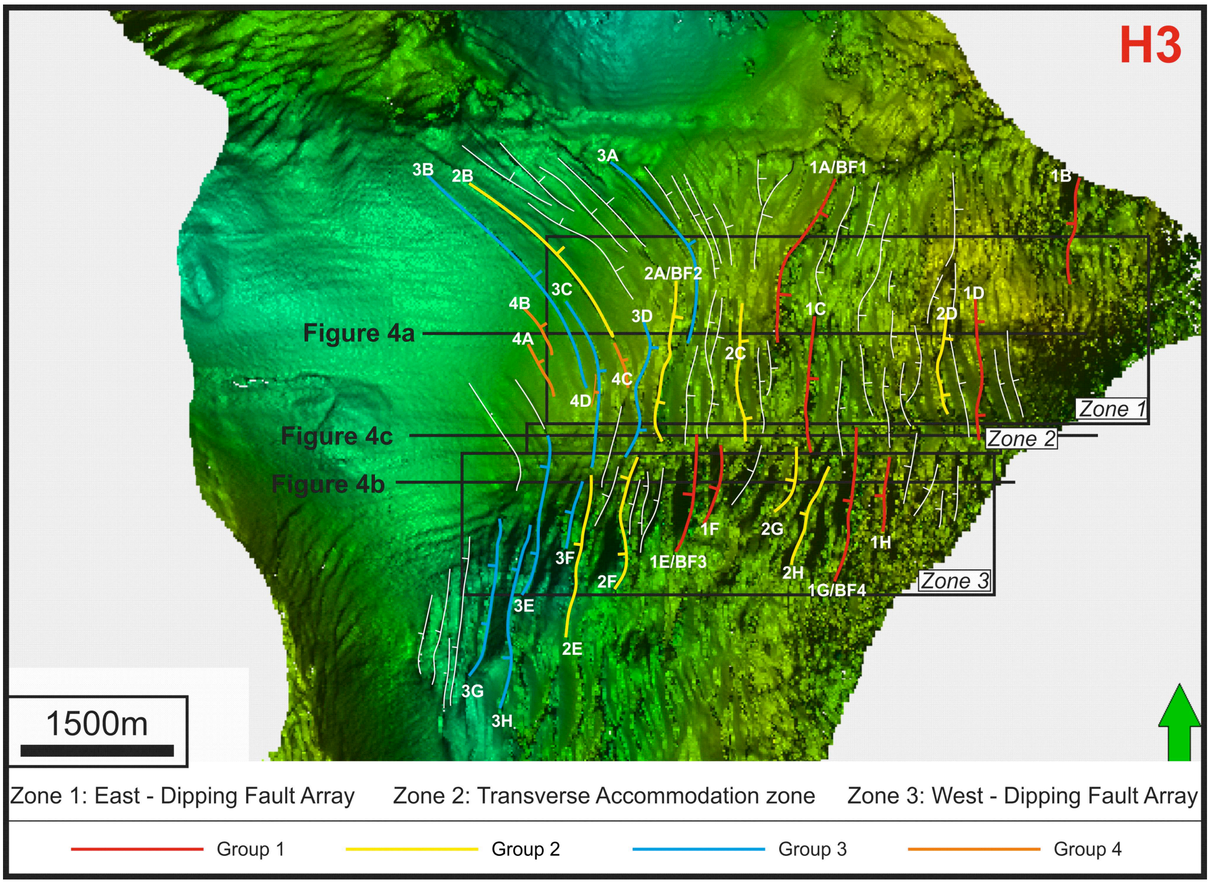
H3
3B
2B
3A
1A/BF1
1B
2A/BF2
3C
4B
3D
1C
1D
2D
Figure 4a
4A
2C
4C
4D
Zone 1
Figure 4c
Zone 2
Figure 4b
1F
2G
1H
3F
1E/BF3
2H
2F
1G/BF4
Zone 3
3E
2E
3G
3H
1500m
Zone 1: East - Dipping Fault Array
Zone 2: Transverse Accommodation zone
Zone 3: West - Dipping Fault Array
Group 1
Group 2
Group 3
Group 4

Figure 3

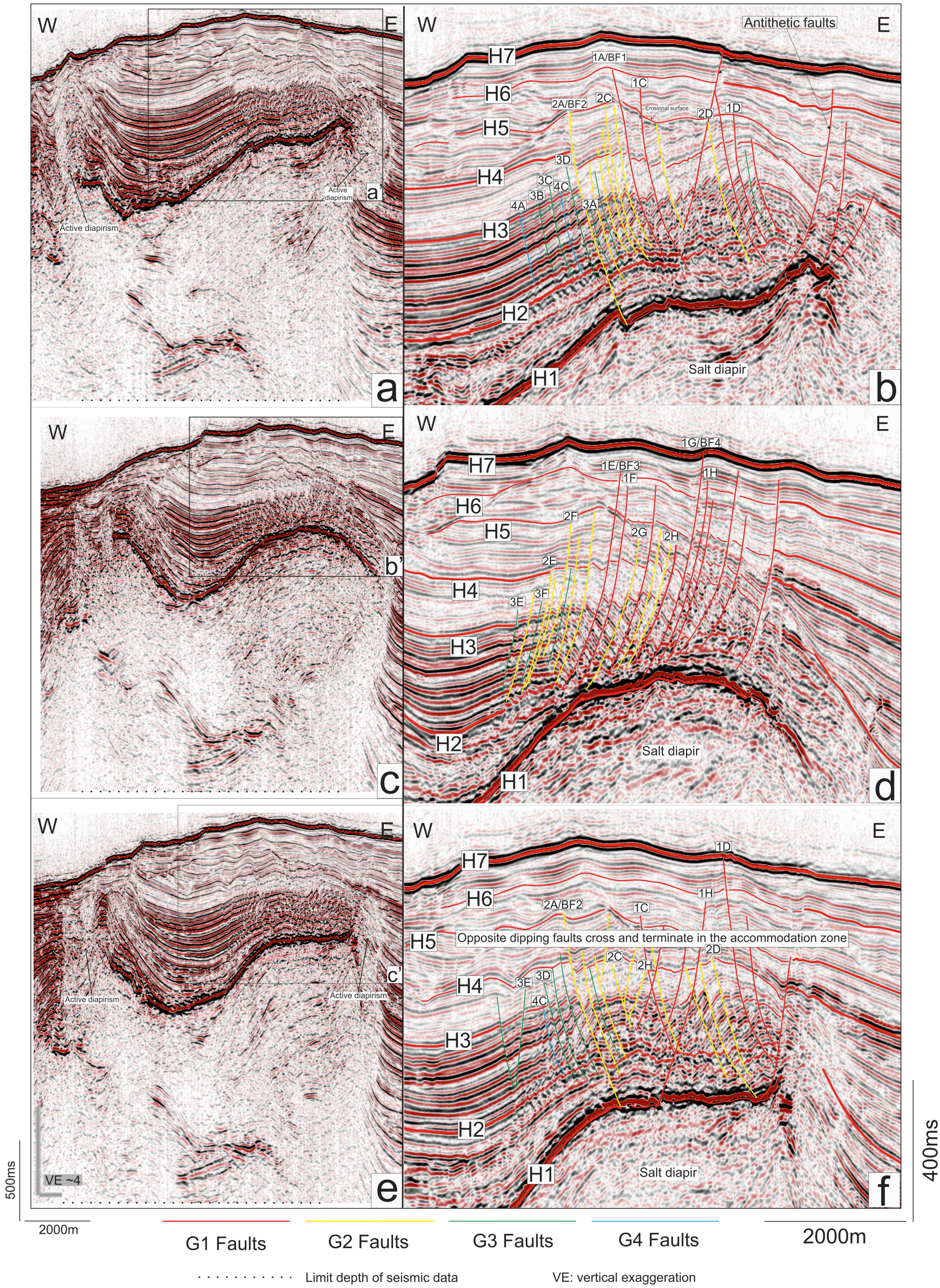
W
E
Active diapirism
Active diapirism
a'
a
Antithetic faults
H7
H6
H5
H4
H3
H2
H1
1A/BF1
1C
2A/BF2
2C
Erosional surface
2D
1D
3D
3C
4C
3B
4A
3A
Salt diapir
b
b'
c
1G/BF4
1E/BF3
1F
1H
2F
2G
2H
2E
3F
3E
d
Active diapirism
Active diapirism
c'
VE ~4
500ms
2000m
e
Opposite dipping faults cross and terminate in the accommodation zone
f
400ms
2000m
G1 Faults
G2 Faults
G3 Faults
G4 Faults
Limit depth of seismic data
VE: vertical exaggeration

Figure 4

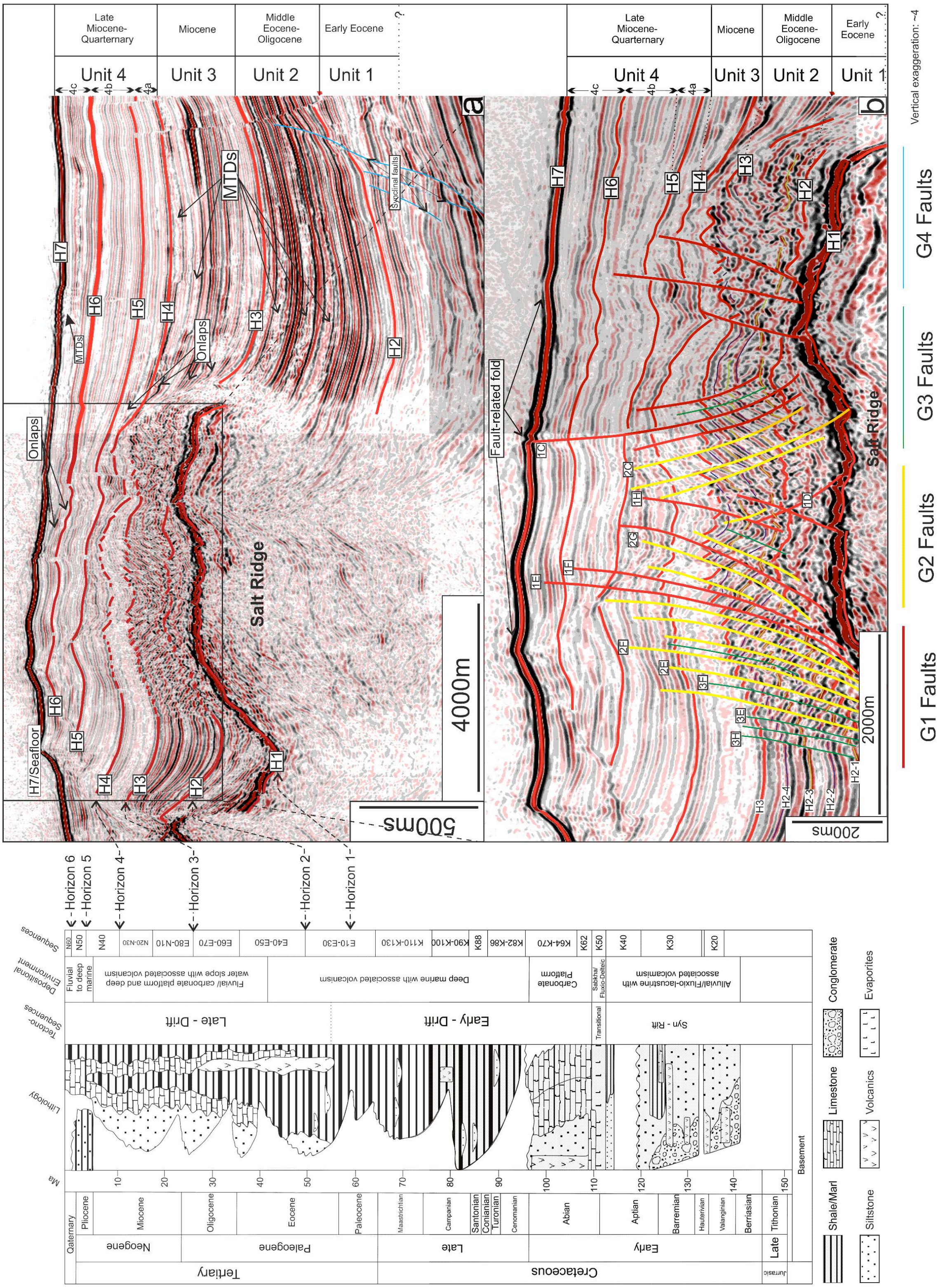
Late Miocene-Quarternary
Miocene
Middle Eocene-Oligocene
Early Eocene
Unit 4
Unit 3
Unit 2
Unit 1
4c
4b
4a
a
b
H7/Seafloor
H7
H6
H5
H4
H3
H2
H1
MTDs
Onlaps
Synclinal faults
Salt Ridge
4000m
500ms
Fault-related fold
2000m
200ms
Vertical exaggeration: ~4
G1 Faults
G2 Faults
G3 Faults
G4 Faults
Horizon 6
Horizon 5
Horizon 4
Horizon 3
Horizon 2
Horizon 1
Tertiary
Cretaceous
Jurassic
Neogene
Paleogene
Late
Early
Qaternary
Pliocene
Miocene
Oligocene
Eocene
Paleocene
Maastrichtian
Campanian
Santonian
Coniacian
Turonian
Cenomanian
Abian
Aptian
Barremian
Hauterivian
Valanginian
Berriasian
Tithonian
Basement
Ma
Lithology
Tectono-Sequences
Depositional Environment
Sequences
Late - Drift
Early - Drift
Transitional
Syn - Rift
Fluvial to deep marine
Fluvial carbonate platform and deep water slope with associated volcanism
Deep marine with associated volcanism
Carbonate Platform
Alluvial/Fluxio-lacustrine with associated volcanism
Shale/Marl
Siltstone
Limestone
Volcanics
Conglomerate
Evaporites

Figure 5

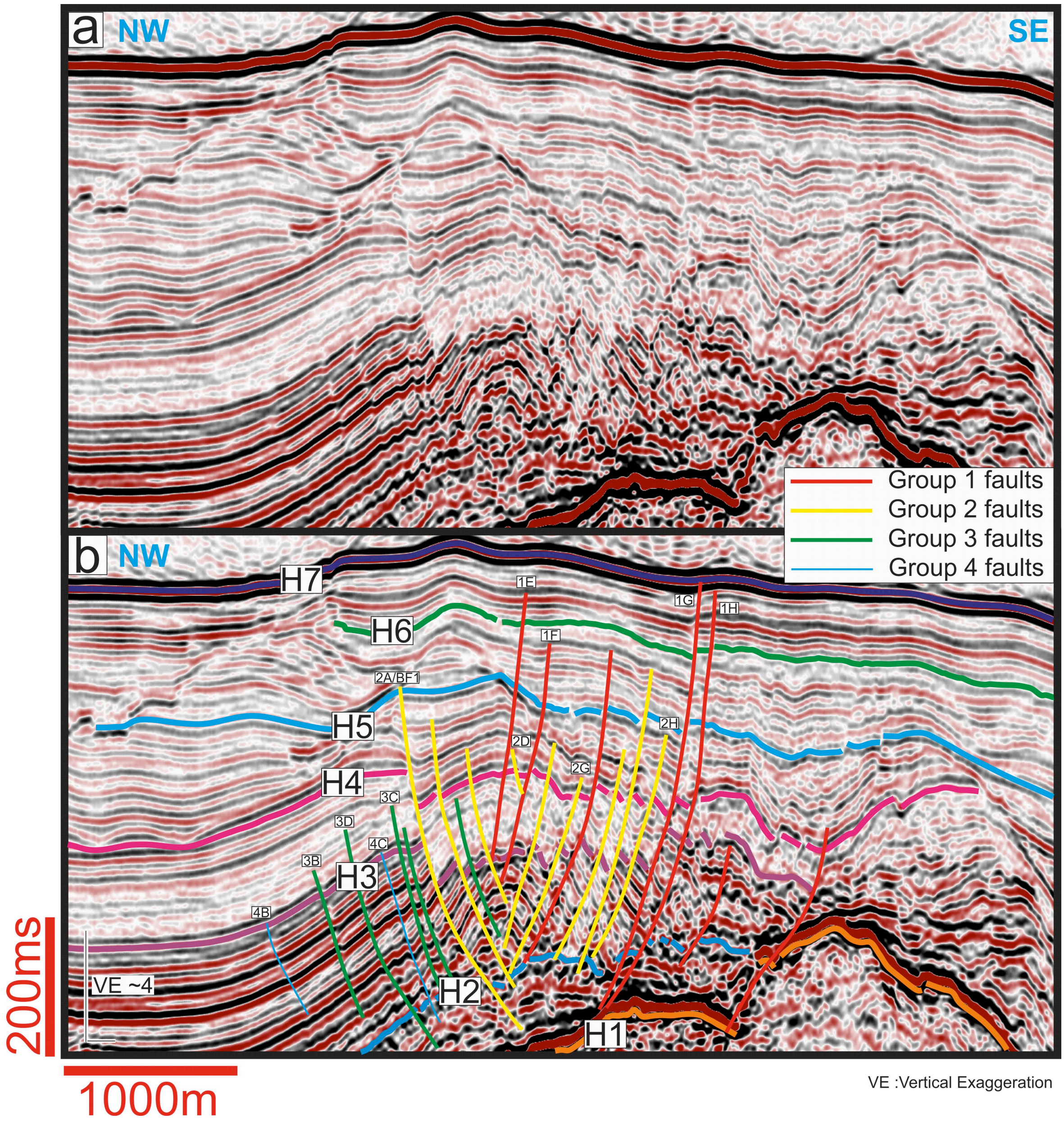

Figure 6

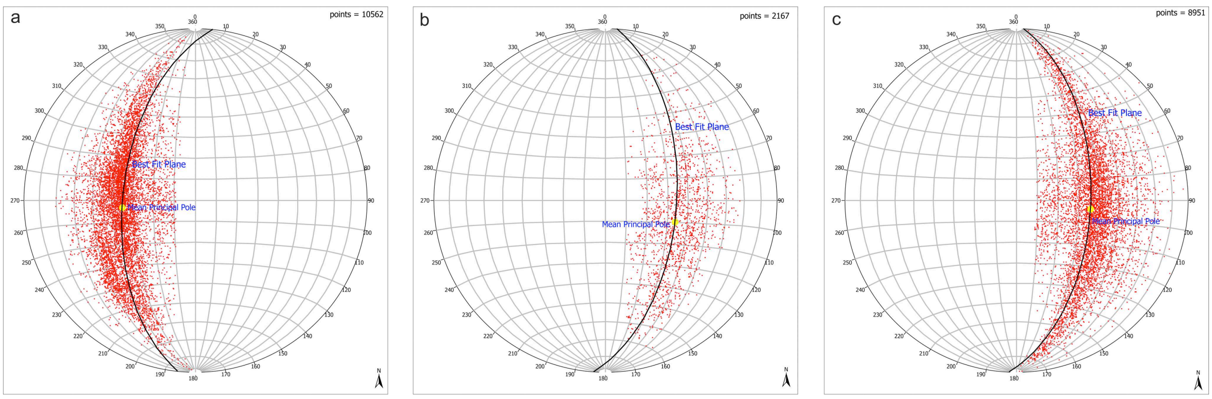

Figure 7

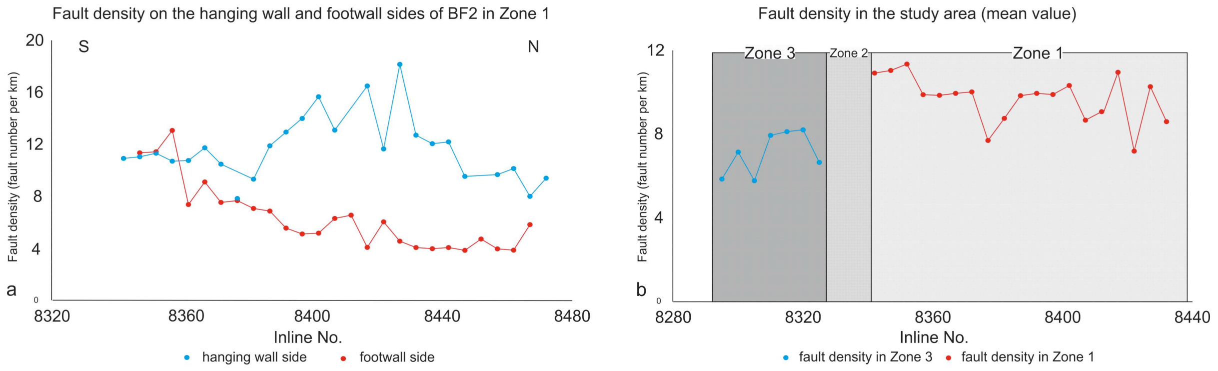

Figure 8

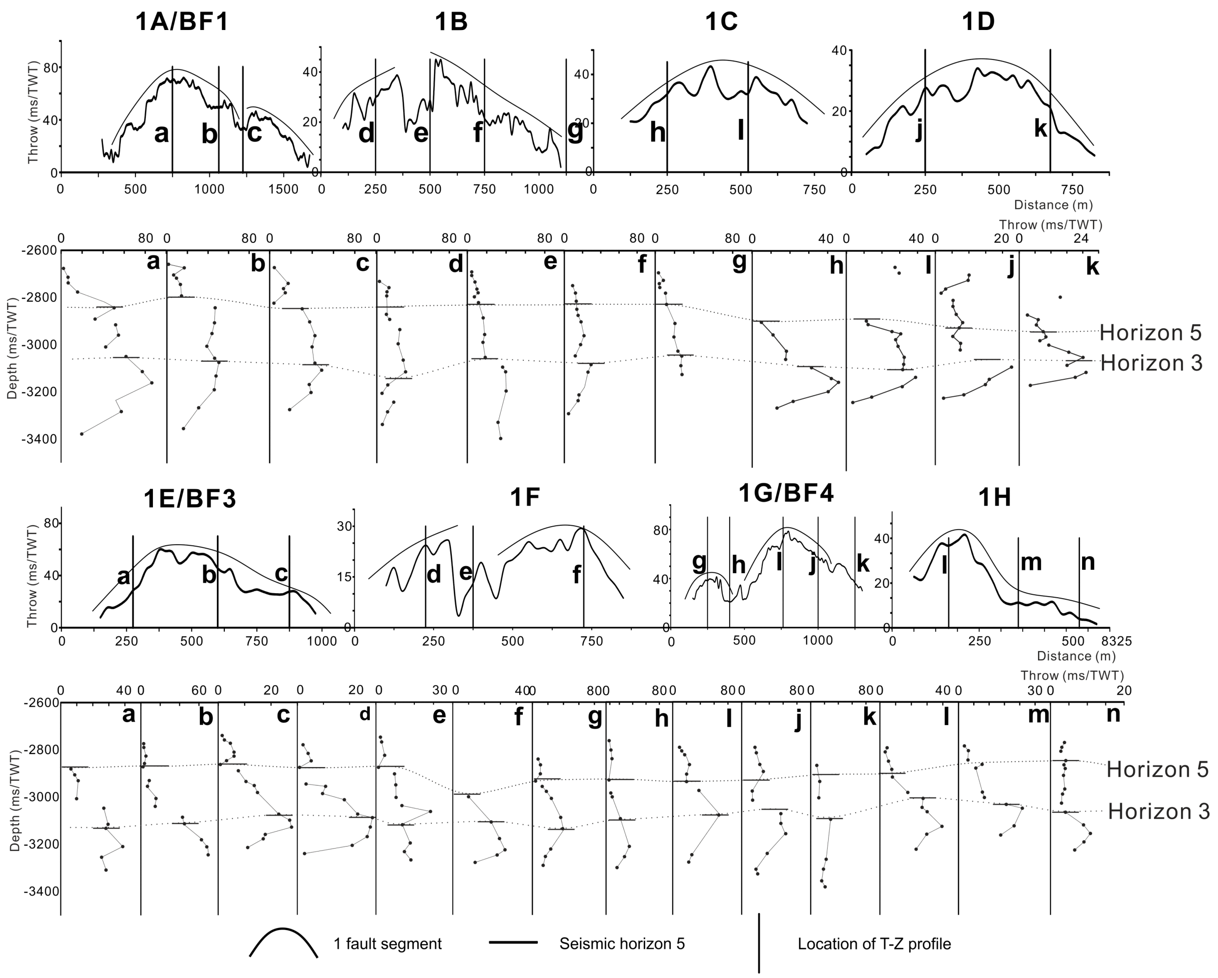

Figure 9

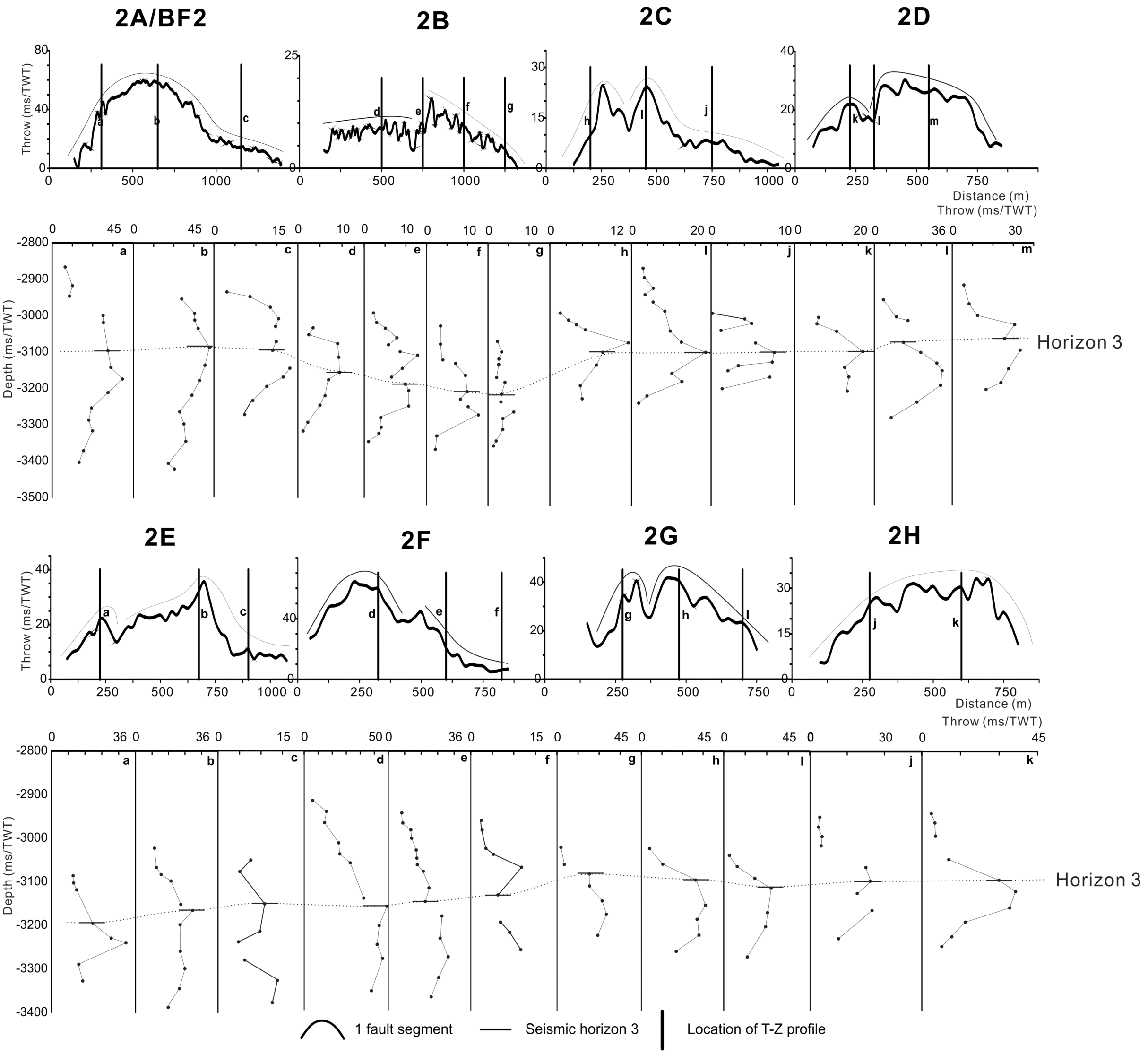

1014

1015 Figure 10

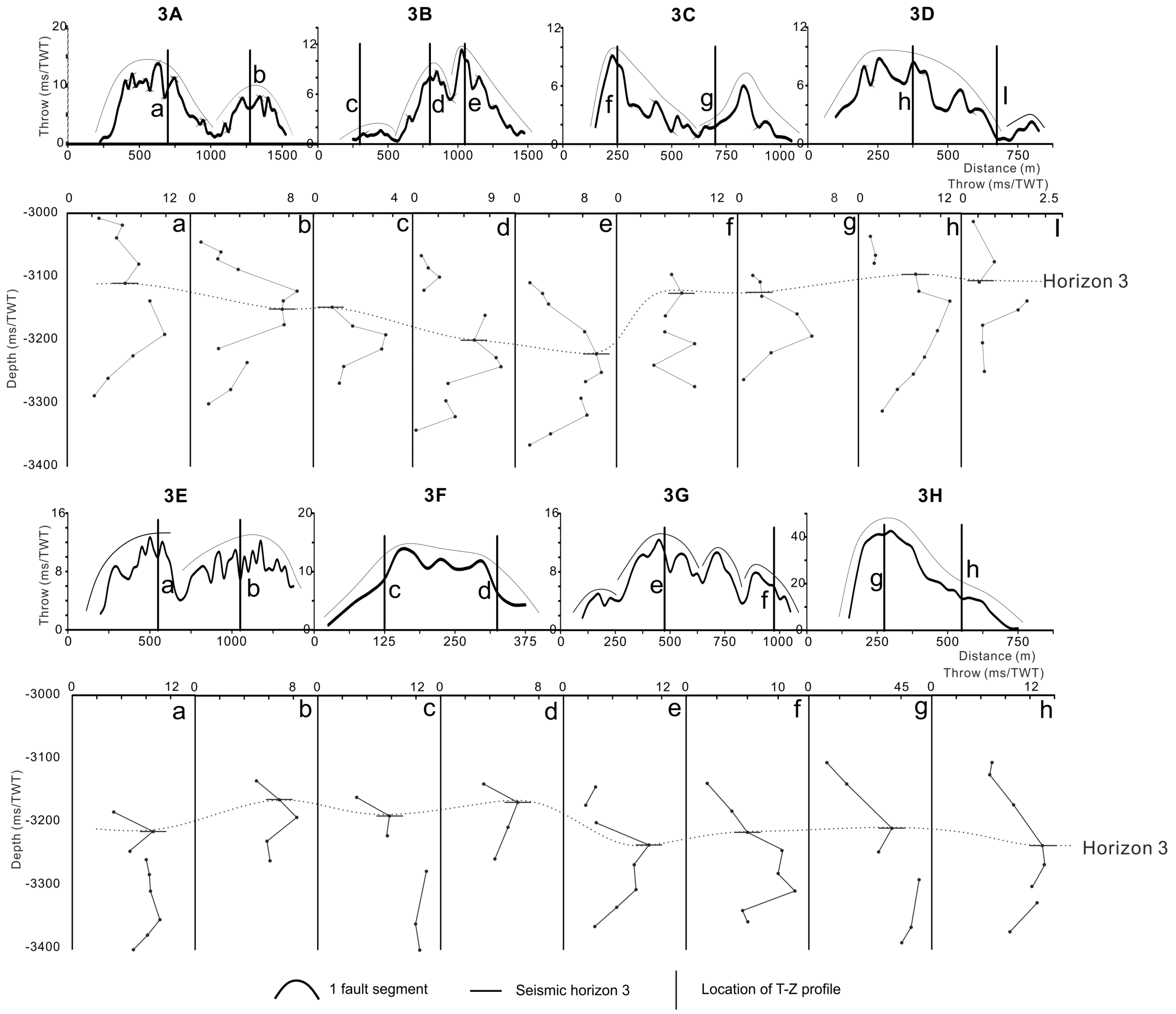

Figure 11

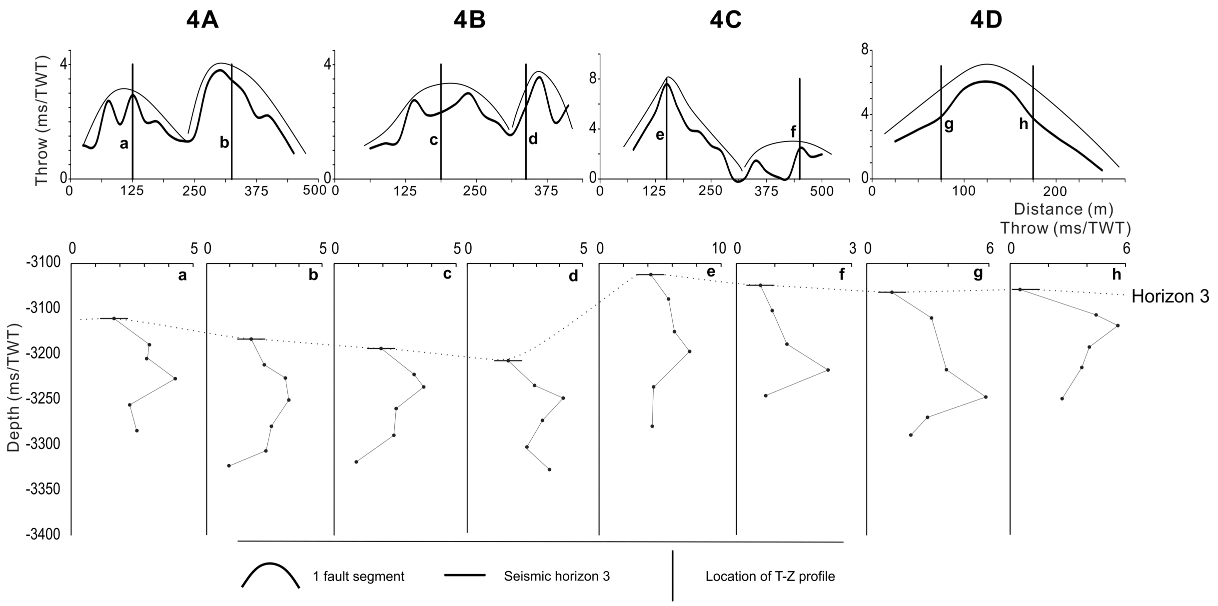

Figure 12

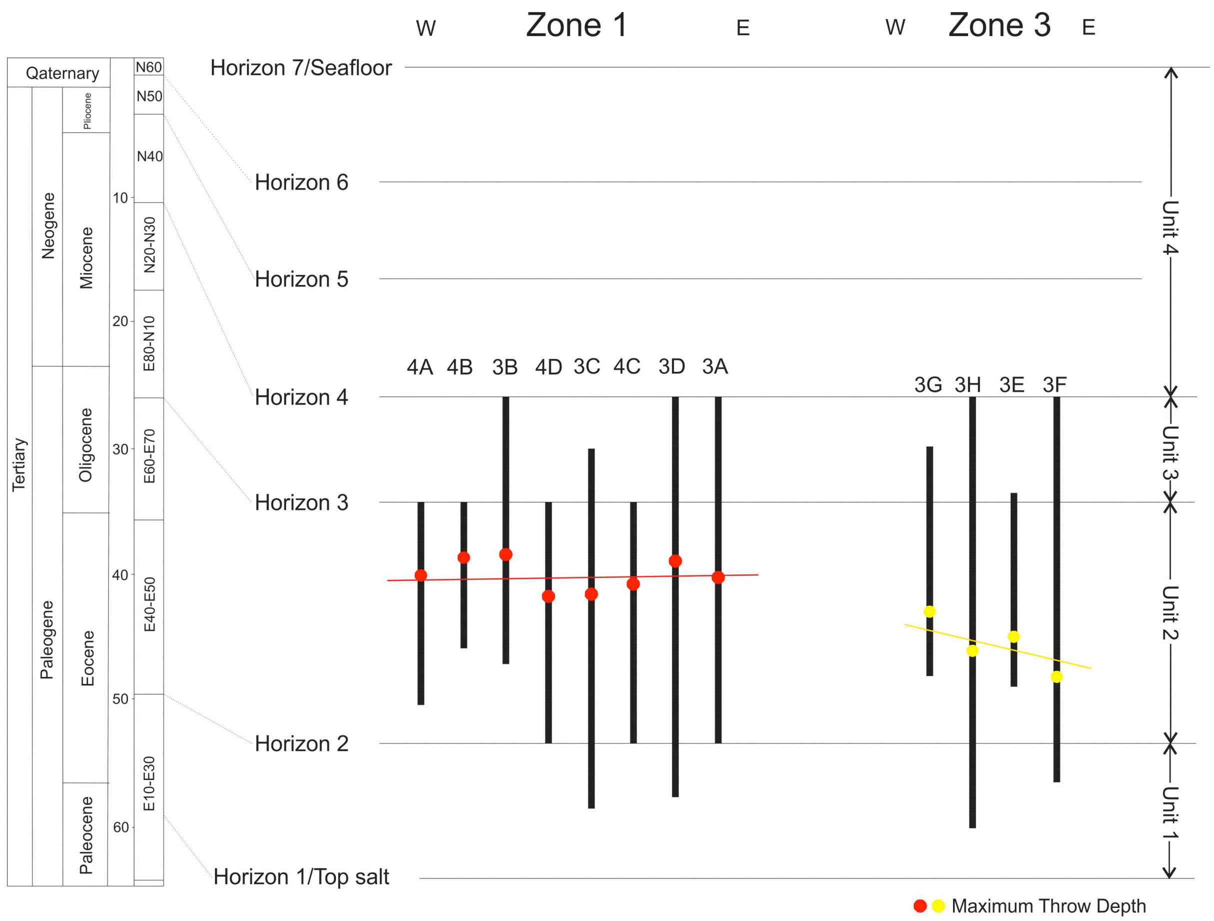
W
Zone 1
E
W
Zone 3
E
Qaternary
Tertiary
Neogene
Paleogene
Pliocene
Miocene
Oligocene
Eocene
Paleocene
10
20
30
40
50
60
N60
N50
N40
N20-N30
E80-N10
E60-E70
E40-E50
E10-E30
Horizon 7/Seafloor
Horizon 6
Horizon 5
Horizon 4
Horizon 3
Horizon 2
Horizon 1/Top salt
4A 4B 3B 4D 3C 4C 3D 3A
3G 3H 3E 3F
Unit 4
Unit 3
Unit 2
Unit 1
Maximum Throw Depth

Figure 13

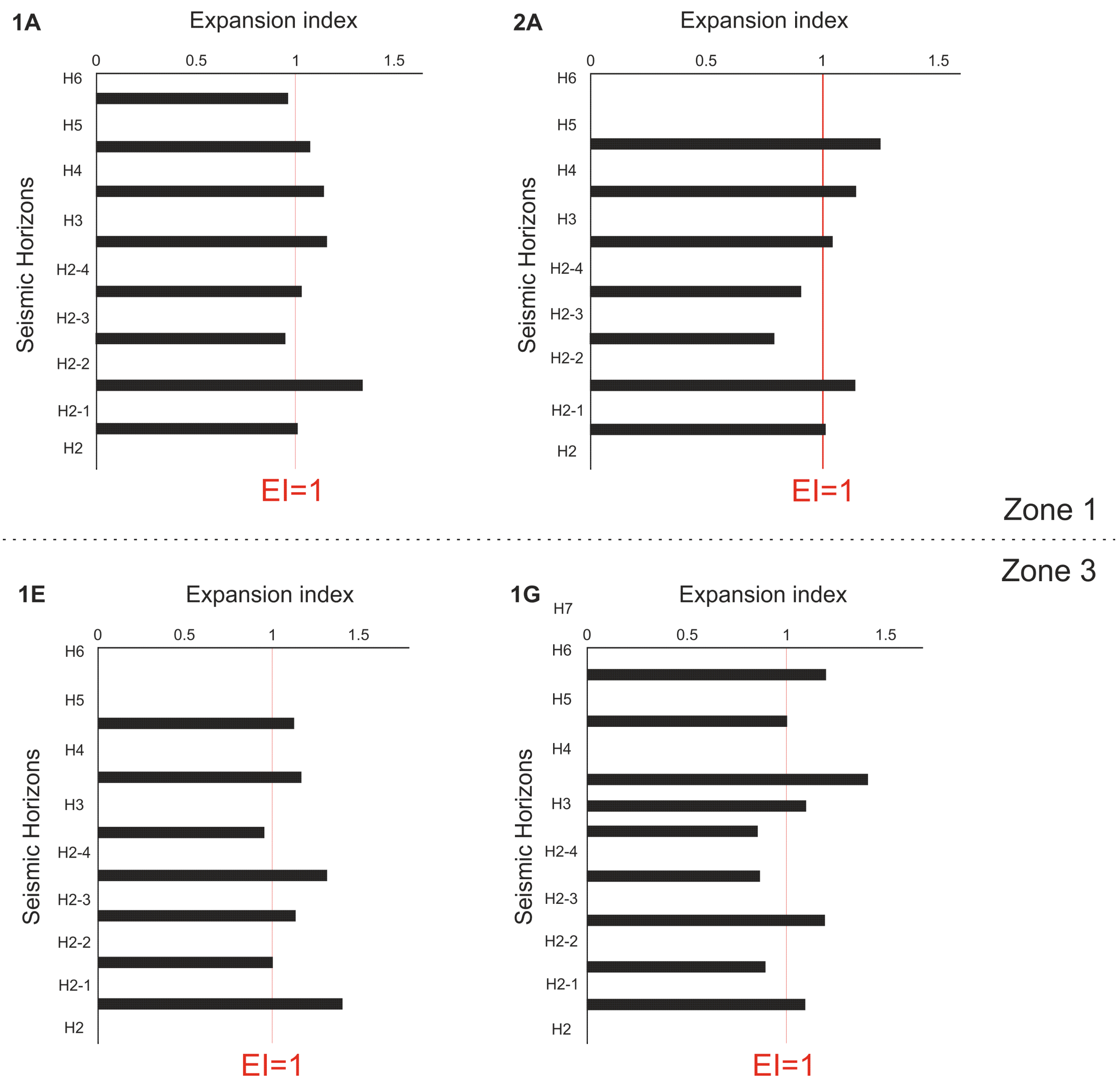

1022

1023 Figure 14

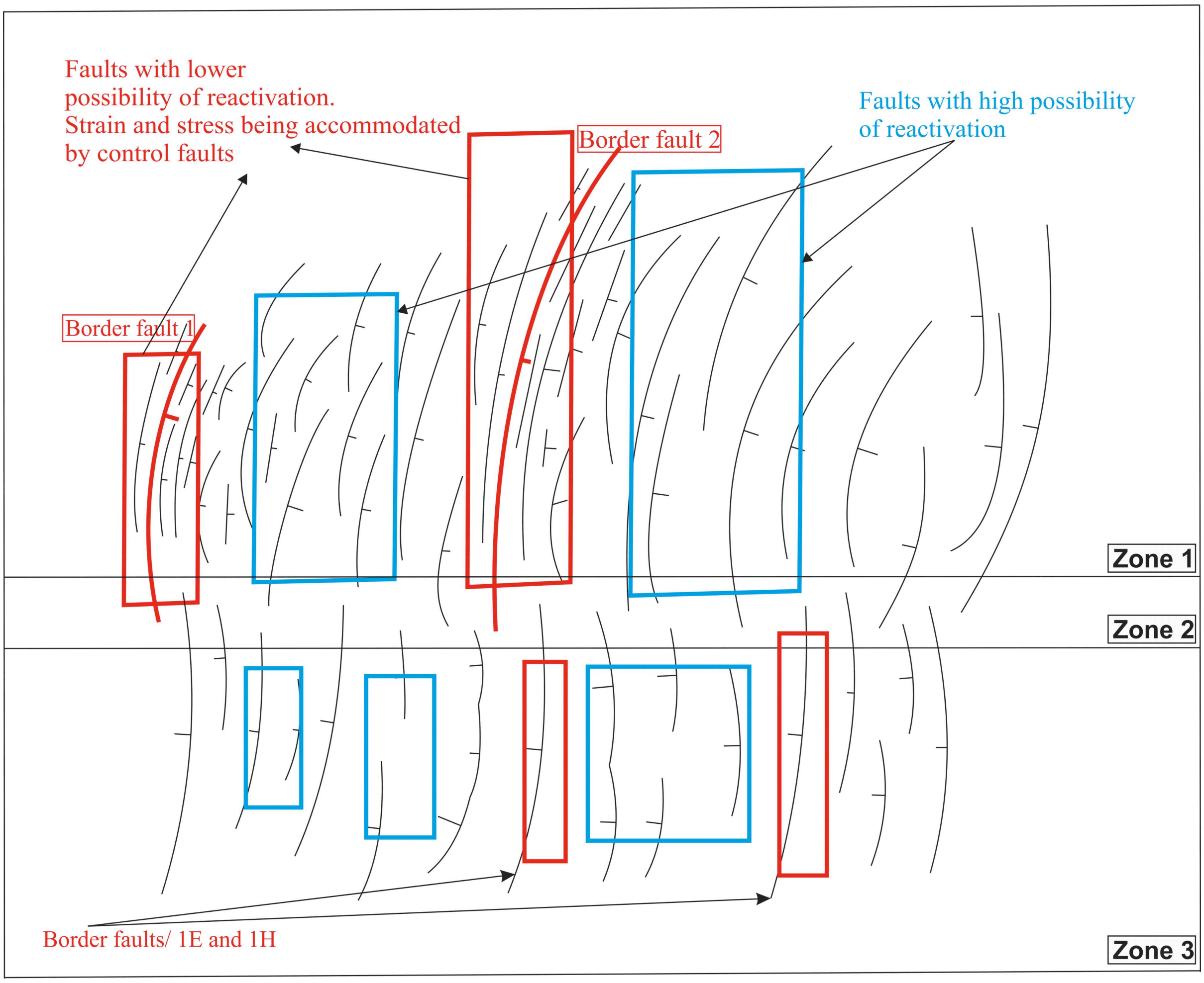
Faults with lower possibility of reactivation. Strain and stress being accommodated by control faults
Border fault 2
Faults with high possibility of reactivation
Border fault 1
Zone 1
Zone 2
Zone 3
Border faults/ 1E and 1H

Figure 15

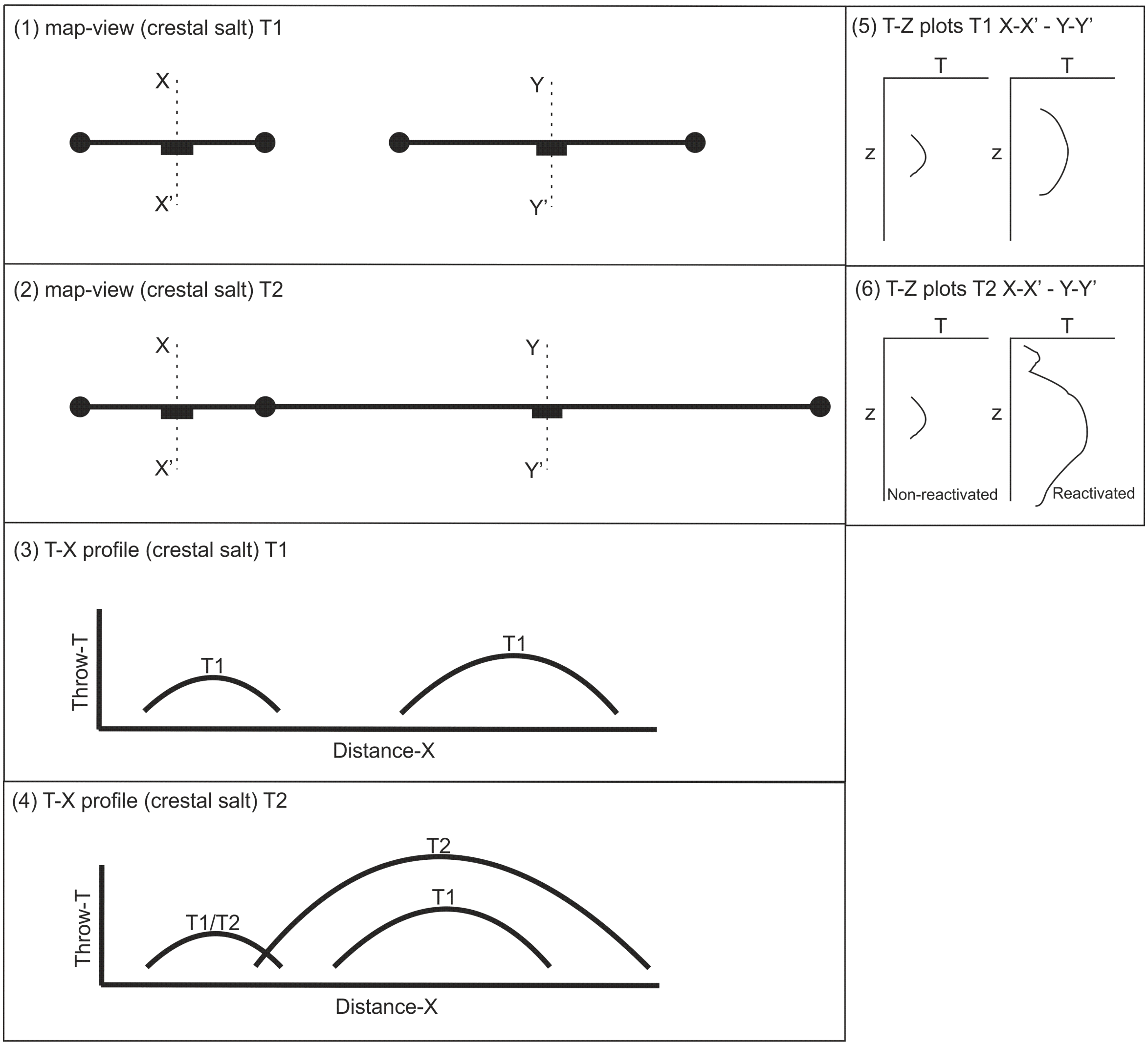

Figure 16

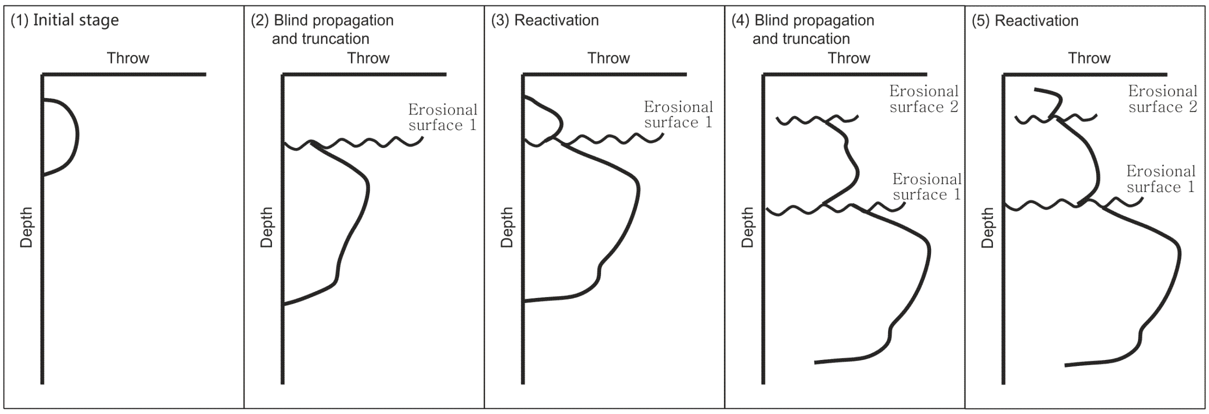

Figure 17

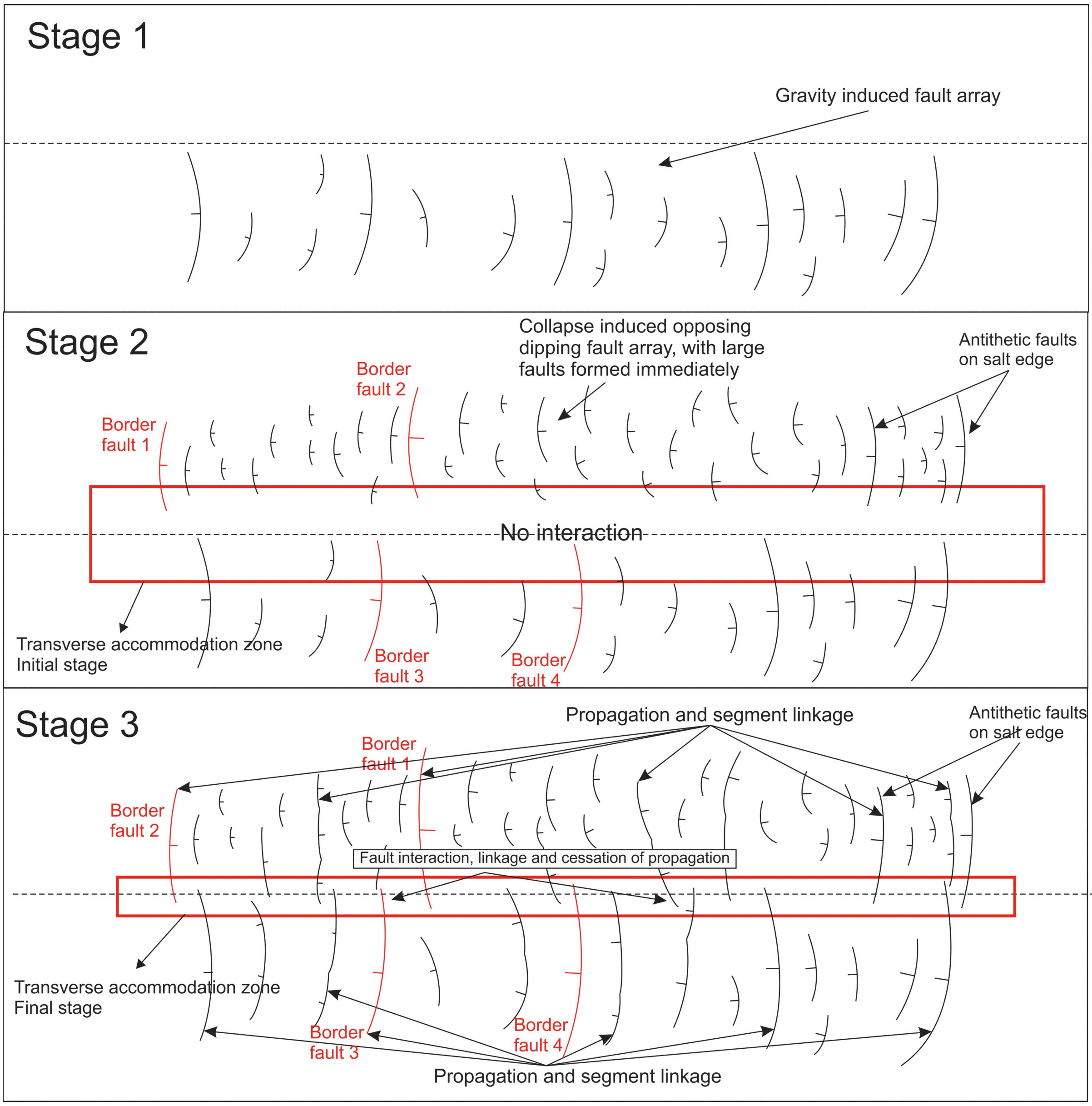

1030

1031 Figure 18

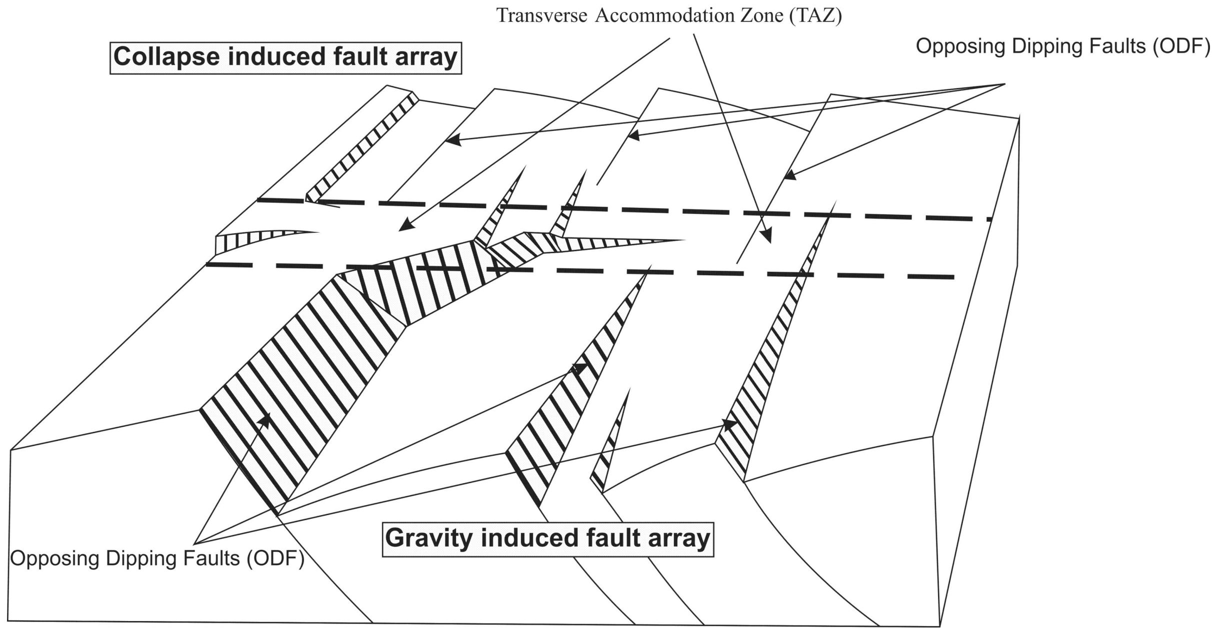

1032

1033 Figure 19